Climate or tectonics? What controls the spatial-temporal variations in erosion rates across the Eastern Cordillera of Colombia?

Helbert García-Delgado, Nicolás Villamizar-Escalante, Mauricio A. Bermúdez, Matthias Bernet, Francisco Velandia

Climate or tectonics? What controls the spatial-temporal variations in erosion rates across the Eastern Cordillera of Colombia?

Helbert García-Delgado, Nicolás Villamizar-Escalante, Mauricio A. Bermúdez, Matthias Bernet, Francisco Velandia

PII: S0921-8181(21)00126-0

DOI: https://doi.org/10.1016/j.gloplacha.2021.103541

Reference: GLOBAL 103541

To appear in: *Global and Planetary Change*

Received date: 1 October 2020

Revised date: 23 May 2021

Accepted date: 8 June 2021

Please cite this article as: H. García-Delgado, N. Villamizar-Escalante, M.A. Bermúdez, et al., Climate or tectonics? What controls the spatial-temporal variations in erosion rates across the Eastern Cordillera of Colombia?, *Global and Planetary Change* (2018), https://doi.org/10.1016/j.gloplacha.2021.103541

Climate or tectonics? What controls the spatial-temporal variations in erosion rates across the Eastern Cordillera of Colombia?

Helbert **García-Delgado**[a,*] hsgarcia@g.syr.edu; helbertgarciad@gmail.com ; Nicolás **Villamizar-Escalante**[b]; Mauricio A. **Bermúdez**[c]; Matthias **Bernet**[d]**;** Francisco **Velandia**[e]

[a]Department of Earth and Environmental Sciences, Syracuse University, Syracuse, NY, USA

[b]Dirección de Asuntos Nucleares, Servicio Geológico Colombiano, Bogotá, Colombia

[c]Escuela de Ingeniería Geológica, Universidad Pedagógica y Tecnológica de Colombia (UPTC), Sogamoso, Colombia

[d]Institut des Sciences de la Terre, Université Grenoble Alpes, CNRS, Grenoble, France

[e]Escuela de Geología, Universidad Industrial de Santander, Bucaramanga, Colombia

[*]**Corresponding author.**

Abstract

Linking the long-term with the short-term exhumation history of a mountain range is vital for understanding the evolution of orogenic topography. Further, erosion rates could be controlled by the variability of climatic and/or tectonic processes over geological time. For example, in the Eastern Cordillera of the Colombian Andes, until recently climate forcing has been hypothesized as the primary driver of rapid Pliocene exhumation rates. In this contribution, we test this climate forcing hypothesis by integrating geomorphic, seismic, geological and published low-temperature thermochronological (Apatite Fission-Track; AFT), and cosmogenic nuclide (CN) data to quantitatively test the correlation of the spatial patterns of exhumation/erosion with either a tectonic or climatic forcing. From a regional perspective, both the long- and short-term erosion rates (derived from AFT and CN data, respectively) have a reasonable correlation with the seismic strain rates and local relief, whereas the contribution of the short-term rainfall patterns to exhumation (and denudation) is either weak or non-existent. For the Eastern Cordillera, tectonism through seismic deformation therefore seems to be a more critical driver of the topographic evolution of the range when compared with the climate variable. To deepen our investigation, we subdivided the study area into six subregions and performed a detailed statistical analysis. In one out of the six subregions (SEC2E), in the Quetame Massif area, short-term rainfall data is well correlated with the computed erosion rates. Nevertheless, the ten-fold difference between the long-term (2.36 km/Myr) and the current (0.27 km/Myr) denudation rates suggest they are strongly decoupled. The remaining five subregions featured varied correlations suggesting that the tectonic-climatic characteristics of each area must be considered and that effective local controls, such as rainfall in subzone SEC2E, cannot be extrapolated to the whole range. Finally, we discuss the tectonic implications of our findings, stressing how tectonic inheritance, typical of inversion orogens such as the Eastern

Cordillera, is critical for understanding the spatial variability in exhumation/erosion rates and surface uplift. For instance, we reconstructed the paleoprofiles of four rivers (the Duda, Ariari, Guayuriba, and Guatiquía Rivers), draining the Sumapaz and Chingaza relict landscapes, on the hanging wall of the Servitá Fault, the typical example of an inverted structure. In this way, we evidenced a net surface uplift of at least 1.4 km since the late Miocene, which we speculate primarily controlled by the Servitá Fault. These findings have first-order implications as they provide evidence for Pliocene to Pleistocene landscape rejuvenation driven by tectonically inverted faults.

Keywords: mountain building, erosion rates, exhumation rates, Northern Andes, Servitá Fault, tectonic inheritance

1. Introduction

Understanding the links between mountainous landscape evolution, its long-term exhumation/erosion history, and short-term denudational rates is critical to recognize actively deforming areas (e.g., Kirby et al., 2003; Kirby and Whipple, 2012; Gasparini and Whipple, 2014; Whipple and Gasparini, 2014; Abrahami et al., 2016), that may entail geological hazards (e.g., Kirby et al., 2008). Even though tectonic activity is often reasoned to be the primary factor controlling deformation history and mountain building (e.g., Burbank et al., 2003; Bermúdez et al., 2013; Gasparini and Whipple, 2014; Godard et al., 2014; Wang et al., 2014), climate could also induce short-term surface uplift through erosional unloading (Willett, 1999; Roe et al., 2002; Stolar et al., 2007; Menéndez et al., 2008; Whipple, 2009). Over the past two decades, growing knowledge of orogen-scale erosion processes led several authors to propose that climate can be a primary conditioning factor of mountain building (e.g., England and Molnar, 1990; Willett, 1999; Montgomery et al., 2001, Montgomery and Brandon, 2002; Reiners et al., 2003; Molnar, 2004; Stolar et al., 2007). In contrast, other authors have favored a decoupling between long-term erosion, short-term erosion and rainfall (e.g., Burbank et al., 2003; Vernon et al., 2009; Abrahami et al., 2016). In the past decade, the discussion around the climatic influence on enhancing exhumation and surface uplift in tectonically active mountain ranges has only intensified (e.g., Herman et al., 2013; Schildgen et al., 2018; Willett et al., 2020).

Likewise, in mountainous regions, the study of climate-landscape-biodiversity relationships can explain biological diversification and species richness (e.g., Antonelli et al., 2018; Salles et al., 2019). The Neogene-Quaternary uprising of the Andes chain, for instance, modified rainfall distribution due to the creation of an orographic barrier (e.g., Kaandorp et al., 2005; Bookhagen and Strecker, 2008) and drove major drainage reorganization events (e.g., Hoorn, 1994, 1995; Albert et

al., 2018, and references therein), which finally modified the sediment flux to the Amazon Basin, leading to the explosion of biodiversity that we observe today (Hoorn et al., 2010). Hence, a comprehensive topographic and seismic analysis, coupled with low-temperature thermochronology data analysis, can provide a valuable quantification of climate-landscape-tectonics feedbacks and contribute new information regarding the recent surface uplift history in a specific region (e.g., Kirby and Whipple, 2001, 2012; Wobus et al., 2006; Whittaker and Boulton, 2012; Whipple et al., 2013).

The late Cenozoic relationships between exhumation, climate and tectonism in the Eastern Cordillera (EC) of the Colombian Northern Andes (Fig. 1) are still a matter of debate (see recent reviews in Bermúdez et al., 2019; Restrepo-Moreno et al., 2019; Pérez-Consuegra et al., 2021). The long-term exhumation/erosion history of the EC has been constrained with a substantial amount of low-temperature thermochronological data (Apatite Fission-Track, AFT) and Zircon U-Th/He (ZHe) ages; e.g., Shagam et al., 1984; Parra et al., 2009a, 2009b; Mora et al., 2010a, 2015; Siravo et al., 2019a). The EC thermal history shows three main exhumation events: (1) in the Paleocene - Eocene along the present boundary between the Magdalena Valley hinterland basin and the western foothills (e.g., Parra et al., 2012; Caballero et al., 2013a); (2) during the Oligocene (e.g., Gomez, 2001; Parra et al., 2009b), and (3) in the Miocene-Pliocene (the Andean Orogeny), which represents the event responsible for the topographic construction of the orogen (e.g., Parra et al., 2009a, 2009b; Mora et al., 2010a; Ramirez-Arias et al., 2012). This latter exhumation event is also observable in other Northern Andean sectors, such as in the neighboring Mérida Andes (Kohn et al., 1984; Bermúdez et al., 2010; 2011; 2013; 2017). Several authors (e.g., Mora et al., 2008; 2013) have argued for a link between climate and the long-term exhumation of the EC. These authors proposed that climate-driven exhumation occurred during the past 3 Ma, which eventually influenced the asymmetry of the range (Fig. 1A). According to these authors, during Miocene-Pliocene times, the EC's continuous topographic growth formed an orographic barrier that trapped Amazonian wet winds, enhancing high rainfall patterns on the eastern side of the EC and drier patterns in the axial and western foothills. The focused rainfall would therefore be sufficient to increase erosion rates along the eastern foothills (in the Quetame Massif, on the hanging wall of the Servitá Fault), leading to fluvial unloading and short-wave uplift (Mora et al., 2008, 2015). These observations agree with an Andes topographic analysis that found positive spatial correlations between erosion, current-day rainfall, and range morphology (Montgomery et al., 2001). In contrast, catchment-wide erosion rates using ^{10}Be terrestrial cosmogenic nuclides (erCN) for the central EC (Struth et al., 2016) suggest that climate, related to short-term rainfall variability, is a secondary

factor controlling landscape evolution, and that crustal shortening and further thickening represent the primary driver of the observed EC asymmetry.

Figure 1. A. Shaded relief map of the EC of Colombia (with its regional location shown in the upper-right inset) showing the main physiographic domains. The location of the swath profiles is also shown (SEC1 to SEC4). B. Generalized geological map of the study area showing the main structures (faults and folds). Note the basement rocks (Pre-Cretaceous) cropping out in isolated massifs, such as the Quetame and Santander Massifs. The geological map and the fault pattern was modified from Gómez et al. (2015). NP = Nazca Plate; CP = Caribbean Plate; MA = Mérida Andes; PB = Panamá Block.

This contribution aims to constrain the spatial and temporal variations of long-term exhumation along with short-term denudation rates in the EC of Colombia between the latitudes 3°10'N and 7°N, to assess the importance of tectonic and climatic (short-term rainfall) controls on these. With this approach, we attempt to link the EC's cooling history with the factors controlling the short-term evolution of the current relief. Thus, we test the hypothesis that tectonism rather than climate is the primary driver of the erosional and exhumation patterns recorded in the range, contrary to the current assumptions. Finally, we discuss the regional and local tectonic implications for the relationship between climate and tectonics. For this, we examine the spatiotemporal correlations between AFT-derived erosion rates (erAFT) and erCN, geomorphic indexes (local relief, the hypsometric curve, and the normalized steepness index, ksn), and seismic parameters (brittle strain rate, b-value, energy, and uplift) obtained by extrapolating current strain rate over a 5 Ma period. All these data are condensed on four across-strike regional swath profiles that enable us to discuss and bridge the temporal gap between long- to short-term erosion rates and the uplift of the EC.

2. Geological, geomorphological and climatic setting

2.1 Tectonic setting

The EC is the easternmost branch of the Colombian Northern Andes (Fig. 1A). Its present-day shape was sculpted after the Cenozoic tectonic inversion of a large Mesozoic extensional basin (Roeder and Chamberlain, 1995; Branquet et al., 2002; Mora et al., 2006; Sarmiento-Rojas et al., 2006), framed within the interaction between the Nazca, South American and Caribbean plates. The

EC has been considered a bi-verging fold and thrust belt with faster exhumation rates concentrated on the eastern foothills, which was aided by high denudation rates (Mora et al., 2008, 2013, 2015; Ramírez-Arias et al., 2012). Several authors (e.g., Corredor, 2003; Bayona et al., 2013; Caballero et al., 2013) found the first episode of tectonic inversion to have occurred during the Maastrichtian after studying the spatial and temporal variations of the sedimentary record, proposing a multiphase deformation mechanism associated with convergence subduction of the Caribbean plateau in this stage, and subsequent slab flattening in Eocene times (Bayona et al., 2021). This first pre-Andean event was key to the inversion of basement structures and thick sediment accumulation in both the Llanos and Middle Magdalena basins (Gómez, 2001). During the Andean Orogeny, in the Mio-Pliocene, drastic geodynamic changes were responsible for the complete tectonic inversion of the master normal faults that bounded the EC Mesozoic basin and the uplift of the EC. The tectonic inversion of the inherited structures occurred in a transpressional stress state (Kammer, 1999; Mora et al., 2010a; Tesón et al., 2013). This is evidenced by data presented herein such as focal mechanisms (Fig. 2) and is further supported by borehole data (Mora et al., 2010b; Egbue and Kellogg, 2010). There is currently no consensus on what mechanism was responsible for this tectonic inversion. Proposed mechanisms include the tectonic escape of the Northern Andes following the subduction of the Carnegie Ridge (e.g., Gutscher et al., 1999; Egbue and Kellogg, 2010), the indentation of the Panamá Arc (e.g., Farris et al., 2011), strain partitioning due to the obliquity of the Nazca-South American plates subduction margin (e.g., Taboada et al., 2000; Jiménez et al., 2014), and the Nazca flat slab mechanism since 6 Ma (e.g., Siravo et al. 2019b).

The seismotectonic map for the EC highlights the across- and along-strike changes both in fault type and structural style (Fig. 2). In the eastern foothills, north of latitude 4°30’N, a swarm of seismicity extends from the foothills even beyond the Yopal Fault, responding to a transpressive stress state but with deformation partitioned on reverse/thrust faults. The northern swarm of seismicity may partially reflect a response to the long-lasting aftershocks following the Tauramena Earthquake (Dimaté et al., 2003). South of latitude 4°30’N, shallow seismicity is constrained to the hanging wall of the main structures such as the Servitá and Algeciras faults. Both reverse and strike-slip kinematics are distributed along these structures (Mora et al., 2010a). For instance, the recent Mesetas Earthquake on 24 December 2019 (Mw = 6.0) underscored the right-lateral strike-slip component of the Algeciras Fault north of latitude 3°N (Fig. 2). This is supported by recent seismic-strain rates and DInSAR analysis (Noriega-Londoño et al., 2021). The southern seismicity

between the Algeciras and Río Blanco faults predates the Mesetas Earthquake and may be related to active co-seismic deformation building up the orogen.

In the western foothills, most seismicity is located on the footwall of the Bituima-La Salina Fault System, perhaps related to more advanced structures such as the Honda and Cambao thrusts emplaced at the deformation front (Fig. 2). The present-day tectonic regime in this area is challenging to constrain, given the few focal mechanisms obtained. However, some authors have recognized the dominance of a transpressive stress regime throughout the range (e.g., Kammer, 1999; Taboada et al., 2000; Cediel et al., 2003; Montes et al., 2003, Cortés et al., 2005; Velandia et al., 2005; Acosta et al., 2007; Velandia and Bermúdez, 2018; Velandia et al., 2020), which in turn induces dextral displacements along NE-trending bounding structures. For the axial plateau, most current crustal deformation is distributed by inverted longitudinal structures such as the Boyacá and Soapaga faults north of latitude 5°N (Fig. 2). Although persistent reverse kinematics for these structures are acknowledged (e.g., Kammer, 1996), some shallow focal mechanisms suggest that some dextral slip may be released by these structures, as in both foothills. This sense of kinematics agrees with geodetic and geodynamic analyses performed by several authors (e.g., Pennington, 1981; Trenkamp et al., 2002; Mora-Páez et al., 2019), which reinforce the hypothesis of NNE "escape" of the North Andean Block relative to stable South America. A published paleomagnetic clockwise rotation for the axial plateau also seems to be related to a regional dextral shear (Jiménez et al., 2014; García and Jiménez, 2016). Besides these NE longitudinal regional faults, other NW transverse structures might be considered when analyzing brittle deformation of the EC, based on geomorphological and geological evidence (Gómez, 1991; Ujueta, 2014; Velandia and De Bermoudes, 2002; Bayona et al., 2008; García and Jiménez, 2016).

2.2 Geological and geomorphological setting

The EC is built on a crystalline basement composed of Precambrian to Lower Paleozoic metamorphic rocks and Jurassic intrusive rocks cropping out in several isolated massifs (e.g., the Quetame and Santander Massifs, Fig. 1B). A thick succession of Mesozoic to Paleogene sedimentary rocks unconformably covers this igneous-metamorphic core-complex, as well as isolated patches of Paleozoic sedimentary rocks, folded and thrusted because of the Andean orogeny (Fabre, 1983; Cooper et al., 1995).

Figure 2. Seismotectonic map of the EC. Based on the dominant stress state inverted from most of the focal mechanisms, the stress state for the eastern foothills is transpressive. Strike-slip faulting

prevails south of latitude 4°30'N, whereas reverse/thrust faulting dominates north of this latitude along the Guaicaramo thrust. This map also shows the different locations of seismic swarms, which are restricted to the hanging wall of the Servitá-Algeciras faults south of latitude 5°N, whereas to the north the seismic swarm migrates toward the foreland through underthrusting. Note the location of the recent Mesetas Earthquake (24 December 2019, Mw = 6.0), which was closely related to the Algeciras Fault. Fault numbering is as in Figure 1. Seismic data gathered from the National Seismological Network of Colombia, operated by the Colombian Geological Survey (CGS). Only earthquakes with depths < 15 km were included (n = 14,311). Focal mechanisms were gathered from the Focal Mechanism and Moment Tensor catalogue of the CGS (http://bdrsnc.sgc.gov.co/sismologia1/sismologia/focal_seiscomp_3/index.html), the Global CMT Catalogue (https://www.globalcmt.org/CMTsearch.html) and Salcedo et al. (2001).

Geomorphologically, the EC has a curved shape with a NE-SW trend up to ~ 6.2°N, where the regional strike changes to an NW-SE direction (Fig. 1). In this zone, the range exhibits the highest elevations at the Sierra Nevada del Cocuy (SNC). This curved shape of the range has been demonstrated to represent a primary arc instead of an orocline (Jiménez et al., 2014). Regarding the EC asymmetry, recent work using thermochronological data suggested a climate-forcing model, where enhanced rainfall caused by an orographic barrier controlled the mid-Pliocene to present tectonic mass flux (Mora et al., 2008, 2015; Ramirez-Arias et al., 2012). In this model, climate-driven denudation was favored by focused rainfall on the windward side of the orogen, i.e., on the eastern foothills, which induced erosional unloading, prompting faster deformation on the main inherited structures such as the Servitá Fault.

The EC presents three geomorphologic domains: the axial domain and the foothills (eastern and western). These three domains are quite different, not only because of their geological evolution but also in their geomorphological characteristics. The axial area, usually known as the Bogotá Plateau or Altiplano, is mostly composed of Lower Cretaceous shales and Upper Cretaceous to Paleogene sandstones (Fig. 1B). The morphology of the axial zone is dominated by topographic highs that coincide with asymmetric anticlines separated by broad synclines, which formed a significant depression filled with Plio-Quaternary fluvio-lacustrine sediments. These sediments deposited within the so-called Bogotá Basin (Fig. 1B) reach around 600 m in thickness in some areas and record the environmental evolution of the axial domain over the past 6 Ma (Andriessen et al., 1993).

The eastern and western foothills are geologically and geomorphologically different from the axial domain and each other, with the eastern foothills being steeper and shorter than the western foothills (Fig. 1A). In the eastern foothills, Cretaceous shale and sandstone units crop out as in the western foothills. However, the most significant difference between these domains is the pre-Cretaceous rocks exposed in the hanging wall of inversion structures in the eastern foothills (Fig. 1B). Selective reactivation of inherited normal faults since the Paleogene dictated which structures underwent complete tectonic inversion (e.g., Servitá and La Salina fault) (Moreno et al., 2013; Tesón et al., 2013).

3. Pliocene to present-day climatic setting of the EC

Climatic studies related to the building of the EC cover the Late Miocene-Quaternary interval. Most of these were carried out by analyzing glacial and fluvio-lacustrine sediments deposited in the Bogotá and Amazonian basins. During the Quaternary, sharp climatic fluctuations were recorded in the axial basins and are responsible for the environmental evolution in this part of the range (Hooghiemstra, 1989; Andriessen et al., 1993; Hooghiemstra and van der Hammen, 1993; van der Hammen and Hooghiemstra, 2003; Torres et al., 2005). The onset of glaciations at 2.7 Ma marked a new period of intense erosion and landscape modeling, especially in the axial domain, where the highest elevations can be observed (Andriessen et al., 1993). Since the Pleistocene, glaciers existed in several regions, such as the Páramo de Sumapaz and Páramo de Chingaza, all these areas exceeding 3.7 km in elevation (Fig. 1A). The chronological and sedimentological characterization of moraine deposits revealed that glaciers were typical during the Pleistocene at altitudes above 3.5 km (van der Hammen, 1974; Helmens, 1988; Andriessen et al., 1993; Helmens et al., 1997), however some exceptions have been reported (as low as 3 km, Sarmiento et al., 2008). The glacial activity in the Quaternary left behind some remarkable geomorphic features such as U-shaped valleys, hanging valleys, glacial lakes, and extensive moraine deposits (Helmens, 1988; Andriessen et al., 1993).

During the Late Pleistocene-Holocene interval (van der Hammen and Hooghiemstra, 2003), global climate change events such as the Younger Dryas (locally known as the El Abra stadial) were recorded in lacustrine sediments (Kuhry et al., 1993; van der Hammen and Hooghiemstra, 1996). The El Abra stadial to Holocene transition marks the time when the present-day climate of the Colombian Andes was established, including the current temperature and rainfall pattern (van der Hammen and Cleef, 1992). At this time, most glaciers also disappeared from the EC, with the

remainder isolated to the elevated peaks of the SNC. At this time, the EC had reached its present elevation, and had become an effective orographic barrier, trapping the moisture coming from the Amazon rainforest (c.f. Bookhagen and Strecker, 2008). This orographic barrier causes a concentrated high rainfall pattern in the EC's eastern foothills (up to 5300 mm/yr), while the axial domain experiences low annual rates of rainfall (500-1500 mm/yr; Fig. 3). In general terms, rainfall is somewhat higher in the eastern foothills than in the western foothills. Nevertheless, the most remarkable difference lies in the rainfall spot located in the Quetame Massif, where the mean annual rainfall can achieve values above 5000 mm (Fig. 3).

Figure 3. Mean annual rainfall map for the EC. Note the striking orographic effect induced by the range on the foothills, and the high rainfall spot over the Quetame Massif. This map also includes the AFT database classified according to their central age. The reddish boxes correspond to the six subzones where the statistical analysis was performed. See the text for further details. LCA = Los Cobardes Anticline; ArA = Arcabuco Anticline; SNC = Sierra Nevada del Cocuy.

4. Exhumation history of the EC: a synthesis

According to Restrepo-Moreno et al. (2019), a significant quantity of low-temperature thermochronological studies in the Northern Andes have focused on the EC. From the pioneering work of Shagam et al. (1984), Toro et al. (1990) and Van der Wiel (1991), and more recent studies (Gómez et al., 2003; Mora et al., 2008, 2010b, 2015; Parra et al., 2009a, 2009b; Ramirez-Arias et al., 2012; Sánchez et al., 2012; Caballero et al., 2013a; Moreno et al., 2013; Silva et al., 2013; van der Lelij, 2013; 2016; Reyes-Harker et al., 2015; Amaya et al., 2017; 2020; Guerrero, 2018; Siravo et al., 2018, 2019a), the cooling history of the range has been discussed in local and regional terms.

In the northern EC (north of latitude 6° N, at the Santander-Floresta Massif), the cooling history has been sketched by several authors. This history includes at least three significant cooling events, starting in the Late Cretaceous (van der Lelij et al., 2016), followed by a fault-controlled exhumation in the Late Oligocene - Early Miocene driven by the Bucaramanga Fault (Amaya et al., 2017, 2020), and a later Miocene to Pliocene diachronous exhumation of several faulted blocks bounded by minor faults (van der Lelij et al., 2016; Amaya et al., 2017). For the Floresta Massif, the cooling history is rather complicated, due to the anomalous thermal gradient (up to 50 °C/km) related to the Paipa-Iza volcanic complex (Alfaro-Valero et al., 2020). Recent zircon U-Pb and ZFT data show that this complex was active from the latest Miocene and throughout the phase of rapid

surface uplift of the Eastern Cordillera during the Pliocene, when this mountain belt reached its present-day elevation (Bernet et al., 2016).

The central EC thermal history also shows three main cooling events, starting at the Paleocene - Eocene (Gomez, 2001; Parra et al., 2012; Sánchez et al., 2012; Caballero et al., 2013a; Moreno et al., 2013; Reyes-Harker et al., 2015) along the present boundary between the Magdalena Valley hinterland basin and the western foothills, which represents the first stage of tectonic inversion of the proto-EC. During the Oligocene (Gomez, 2001; Parra et al., 2009b; Moreno et al., 2013; Silva et al., 2013) and throughout the Miocene, a rapid exhumation pulse (Parra et al., 2009a, 2009b; Mora et al., 2010a; Ramirez-Arias et al., 2012; Sánchez et al., 2012; Caballero et al., 2013a; Silva et al., 2013) was coeval with the collision and onset of exhumation in the Panamá arc (Farris et al., 2011). Although several authors have related the Miocene event with the indentation of the Panamá – Chocó Block (e.g., Amaya et al., 2017), a flat-slab mechanism was proposed by Siravo et al. (2019b) to explain the topographic construction of the SNC. A final cooling event was recorded for the Pliocene - Pleistocene period (Mora et al., 2008; Parra et al., 2009b; Caballero et al., 2013a; Moreno et al., 2013; Guerrero, 2018). This later event was particularly rapid in the eastern foothills of the range (Fig. 3), at the Quetame Massif (Fig. 2), where Mora et al. (2008) first proposed their climate model for the range.

5. Methods

5.1 Low-temperature thermochronological data and long-term erosion rates

For this study, we compiled a total of 312 published AFT ages (Supplementary Table S1). Due to the lithological variability (mineral fertility) and local fault patterns, differences in central ages reported in these studies can represent a complex cooling history. For instance, in sedimentary rocks, fission-track ages older than the depositional age represent the cooling age from the source of the grains (Reiners and Brandon, 2006; Bernet, 2019). In the present study, we are not interested in older cooling histories but rather the Andean-related thermal evolution; for this reason, we filtered those data with a source signal. Finally, this filtering was complemented with the aim of the P (χ^2) test results. Based on this test, values >5% define a single age population (Galbraith, 1981; Green, 1981), representing a fully annealed apparent cooling age (Supplementary Table S1). As AFT data is better distributed across the study area (Fig. 3), we prefer this thermochronometer for the regional analysis over the currently spatially more limited zircon or apatite (U-Th)/He data. Nevertheless, we also compiled this data and display them in the swath profiles below (See the Supplementary Tables S2 and S3).

The long-term erosion rates (>10^6 yr) were determined using the 1-D thermal advection model age2edot (Brandon et al., 1998; Ehlers et al., 2005) and the compiled and filtered AFT data. Model input parameters assume a normal gradient of 30 °C/km across the study area and a mean surface temperature of 10 °C for the EC during exhumation and surface uplift. Further input parameters include an activation energy for 50% annealing of 147.2 Kj/mol for apatites of average composition, and an annealing parameter Beta of 2,050,000 s^{-1} (Ketcham et al., 1999). See Reiners et al. (2003) for further details.

Besides obtaining long-term erosion rates based on the AFT data, we compiled catchment-averaged erosion rates derived using ^{10}Be terrestrial cosmogenic nuclides (erCN). This data was provided by Struth et al. (2016). The sampling locations are shown in Figure S1. Fortunately, some of these data were acquired in the same catchments sampled by Mora et al. (2008) for thermochronological analysis (i.e., the Guayuriba and Guatiquía River catchments, Fig. S1).

5.2 Topographic analysis

To investigate the coupling between climate, tectonics, topography and erosion rates, we performed a regional topographic analysis by evaluating several geomorphic metrics in a GIS environment (ESRI ArcGIS 10.5). We used a ~30 m-resolution digital elevation model (DEM) from the ALOS sensor (https://www.eorc.jaxa.jp/ALOS/en/aw3d30/index.htm), later averaged by three cells using the *Focal Statistics* tools in ArcGIS to reduce data noise and some inconsistencies related to deep valleys.

We evaluated several topographic metrics (mean slope, Local Relief (LR), and the Hypsometric Integral (HI)) for the EC that are useful to highlight the erosional state of the topography (Keller and Pinter, 2002) and correlate it with a possible driver (climate, tectonics or both). We computed these topographic metrics by performing regional smoothing with a 5 km-radius moving circle window of a regional DEM. We included not only the EC but also surrounding areas to reduce the effects of edge singularities. The LR corresponds to the difference between an envelope surface connecting the peak elevations and a sub-envelope surface connecting the valley bottoms (Molin et al., 2004). This metric works to recognize deeply incised areas that are frequent in landscapes adjusting to a base level fall induced by recent surface uplift, a climate change in boundary conditions or the presence of low-relief surfaces being incised by surrounding streams (e.g., Scotti et al., 2014; Azañón et al., 2015).

The HI index is the quantification of the area under the hypsometric curve (Pike and Wilson, 1971; Strahler, 1952). The HI index can be expressed as:

HI = (mean elevation – minimum elevation) / (maximum elevation – minimum elevation) (1)

The above equation is useful for understanding the erosional state in a particular landscape. Put differently, it helps to detect areas affected by potential landscape rejuvenation (Bustos et al., 2013). Some authors have explored the use of HI index maps to identify tectonic features evidenced by anomalous spatial distributions of HI index values (e.g., Andreani and Gloaguen, 2016).

Understanding erosional patterns in a particular landscape can be achieved by studying bedrock river dynamics and the continuous interaction between channel gradient and erosion, which often displays non-linear behavior (e.g., Ouimet et al., 2009; DiBiase et al., 2010). In a steady-state landscape, bedrock rivers can be analyzed using a 1-D model, which describes a power-law that correlates the channel slope (S) with the upstream contributing drainage area (A) (Whipple and Tucker, 1999; Kirby and Whipple, 2001; Wobus et al., 2006). This power law is known as Flint's law (Flint, 1974):

$$S = ks * A^{-\theta} \quad (2)$$

where ks is the steepness index, and θ is the concavity. As θ is mostly independent of climate, rock uplift, and lithology, the ks index analysis becomes a very optimal tool to quantify and better comprehend the erosional response of a target landscape (Whipple et al., 2013). The most common way to analyze the ks index is by obtaining a normalized form (ksn) by introducing a reference concavity (θref), which usually ranges between 0.4 and 0.6 (Whipple, 2004; Wobus et al., 2006). The most common value for θref used in the literature and in recent work on the EC is 0.45 (e.g., Struth et al., 2016). The ksn index and its statistics were calculated using the Topographic Analysis Kit (TAK) code for Matlab (Forte and Whipple, 2018) integrated within the Matlab-based software TopoToolbox (Schwanghart and Scherler, 2014), employing a critical drainage area of $1x10^7$ m^2.

5.3 Climate data

In this study, we used processed rainfall data (Fig. 3) from the Tropical Rainfall Measuring Mission (TRMM) that spans from 1998 to 2009 (Bookhagen, 2013) and is freely available for download at http://www.geog.ucsb.edu/~bodo/TRMM/#tif. This data has the advantage that it covers the entire study area with a 0.04°x0.04° cell size, which provides sufficient resolution to detect the regional trends in rainfall, and has also been calibrated with some ground stations.

5.4 Swath Profiles

As the AFT data are not homogeneously distributed across the EC (Fig. 3), we present and discuss the data gathered in four swath profiles. In these swaths, we present the mean topography of the

range, the AFT and erAFT, the LR, the HI, the mean ksn and the mean rainfall. The swaths were generated using the *SwathProfiler* tool for ArcGIS (Pérez-Peña et al., 2017) using a swath-width of 10 km. As swath profiles avoid the classical subjective location issue of cross-sections (Telbisz et al., 2013), they become a useful tool to analyze regional trends in topographic and climate data. The swaths are oriented perpendicular to the structural grain of the EC. A variation of the HI, the Transverse Hypsometric Integral (THi*) index, is also calculated using the *SwathProfiler* tool, and represents a variant of the Hypsometric Integral index (HI) but oriented to give information in this kind of plot (Pérez-Peña et al., 2017).

5.5 Seismic Metrics

In order to quantify the effects of seismicity across the EC, we compiled a seismicity record over the last 27 years (1993–2020) from the National Seismological Network of Colombia. We only considered data with reported local magnitudes Ml. Figure 2 shows a summary of earthquakes (~14,311 reports) that occurred in this area (only earthquakes in the brittle zone < 15 km in depth). Using this seismicity database, we calculated the seismic brittle strain rate, b-values, and the released seismic energy. The seismic energy (Se) from the local magnitudes is calculated using the Gutenberg and Richter (1954) equation:

$$log\ (Se)\ = bM_l + a \quad (3)$$

This equation involves two parameters: the a-value that measures the seismic activity or earthquake productivity, and the *b*-value that describes the relationship between frequencies of small and large earthquakes (Schorlemmer et al., 2005; Cheng and Sun, 2018). The spatial and temporal variations of these two parameters, especially the *b*-value, have been thoroughly investigated (e.g., Smith, 1981; Frohlich and Davis, 1993; Schorlemmer et al., 2005; Godano et al., 2014; Rivière et al., 2018; Wu et al., 2018). The parameters a and b are estimated by a least-squares fit of cumulative magnitude-frequency relationships constructed from subsamples of the seismic database across each polygon in 0.1°×0.1° cells. They are equivalent to the intersect and slope, respectively, of the Gutenberg-Richter relationship (Gutenberg and Richter, 1954).

The seismicity records brittle deformation of the upper crust; the spatial distribution and frequency of earthquakes can be related to the rate of brittle deformation (Holt et al., 2000). Thus, we can use the compiled seismic database to estimate the present-day distribution of brittle strain rate and extrapolate the total amount of seismic strain over timescales more protracted than the observation interval, using the observed earthquake magnitude-frequency (Gutenberg-Richter) relationship. To

achieve this, we use the method described by Braun et al. (2009) and calculate the seismic/brittle strain rate as:

$$\varepsilon_H = \left(\frac{1}{2\mu\Delta V\Delta t}\right)\left(\frac{b10^{a+9.1}}{1.5-b}\right)\left(10^{(1.5-b)M_{max}}\right) \quad (4)$$

where the parameters a and b are defined and calculated as explained above; M_{max} is the maximum observed magnitude; μ is the elastic shear modulus; and ΔV is the volume of the crust (that is, the moving 0.1º×0.1º cell area multiplied by the depth of the maximum magnitude earthquake) in which the earthquakes were observed over a period of time Δt (in this case, Δt = 24 years). Given that the depth of the maximum magnitude earthquakes (30-200 km) generally exceeds the depth of the brittle-ductile transition (~15-20 km), we recalculated seismic strain rates using only earthquakes with hypocentral depths less than 50 km (see Bermúdez et al., 2013 for more detailed information).

According to Braun et al. (2009), we can describe the present-day deformation of the EC mountain range as a geographically variable but vertically uniform horizontal shortening at a rate ε_H. The mass conservation at the scale of the lithosphere (incompressibility) implies that a vertical thickening of the lithosphere must accompany this horizontal shortening at a rate $\varepsilon_V = -\varepsilon_H$ assuming that horizontal deformation in a direction perpendicular to the direction of maximum shortening is negligible. Assuming the compressive component of the transpressive stress state has been dominant in the past 5 Ma and still governs some areas of the range (Fig. 2), we calculate the total amount of thickening experienced across the EC integrating the computed vertical strain rate over 5 Ma as follows:

$$\varepsilon_V = -\varepsilon_H \times 5\ Ma \quad (5)$$

The computed vertical strain can then be used to compute the local lithospheric thickening, and, by assuming local isostatic equilibrium, the amount of seismic uplift, u, experienced by each 1 km × 1 km cell over the last 5 Ma is:

$$u = h_c\varepsilon_v\left(1 - \frac{\rho_c}{\rho_m}\right) \quad (6)$$

In the above expression, h_c is the crustal thickness, and ρ_c (2700 kg m^{-3}) and ρ_m (3200 kg m^{-3}) are the average continental crustal and mantle rock densities, respectively. We used the CRUST1.0 model (Bassin et al., 2000; Laske et al., 2013) to obtain h_c values. We define the seismic uplift *u*, as the amount of vertical thickening of the chain that generates a positive topography (including rock

or surface uplift) predicted from the seismic energy release measured over the past 24 years and extrapolated over the past 5 Ma.

5.6 Statistical analysis: Pearsonian correlation and ANOVA tests

In order to gain insight into the potential controls on erosion and exhumation rates in the EC, two different statistical analyses were performed. First, we calculated Pearsonian correlation coefficients between each of the potential factors (topographic, climatic and seismic) and erosion rates (erAFT and erCN). We seek to avoid subjectivity and test the spatial correlation between these parameters more objectively with this approach. Given that we compare all variables for six areas, correlations are statistically significant (at a 90% confidence level) for a Pearson correlation coefficient $r \geq 0.6$. Second, a multiple regression analysis was accomplished between erAFT and the average measures of those variables where there was a high Pearson's correlation coefficient across all swath sub-zones. We applied a stepwise Akaike Information Criteria (AIC) model (Akaike, 1974) in combination with a one-way analysis of variance (ANOVA) test ($p < 0.05$; Venables and Ripley, 2002). This second method allows us to analyze the response variable (long-term erosion rate, erAFT) according to the behavior of the other variables called predictors.

5.7 Surface uplift in the EC: stream profile reconstruction

To further investigate how inverted structures helped sculpt the EC topography, at the Quetame Massif we reconstructed the paleoprofile of rivers draining the Sumapaz and Chingaza páramos, two low-relief landscapes on the hanging-wall of the Servitá-Algeciras faults. These low-relief areas are commonly known as "relict" landscapes and are useful in long-term landscape analysis because they record ancient topographic conditions (e.g., Clark et al., 2005, 2006; Whipple and Gasparini, 2014). We assume that the Sumapaz and Chingaza páramos are remnants of a formerly more extensive plateau that has undergone recent surface uplift up to its present-day elevation. The uplifted plateau is then affected by substantial fluvial dissection to tear the excess topography apart. This process is driven by an incisional wave migrating upstream and bounded by a major knickpoint that separates the transient low-relief upstream from the rugged canyons downstream. We can therefore estimate the net surface uplift by projecting downstream the paleoprofile currently delimited by the uppermost knickpoint.

To do this, we used the SegmentProjector tool included in the TAK software. This function selects the stream segments to project (bounded downstream by the major knickpoint) and performs a least-squares linear fit on the χ-elevation (or often known as Chi-plot) relationship along with a 95%

confidence interval on this fit. We employed this technique to project the paleoprofiles of the Duda, Ariari, Guayuriba, and Guatiquia Rivers (Supplementary Fig. S1) that eventually drain the Sumapaz – Chinagaza area. Along with the expected surface uplift, the tool allows us to provide the minimum and maximum bound uncertainties for each paleoprofile.

6. Results

6.1 Swath profiles

The topographic swath profile results are shown in Figures 4, 5, 6, and 7. As mentioned above, we compiled several topographic metrics in these profiles, and the corresponding maps are visible in Supplementary Figure S2. In addition to the topographic profiles and the AFT analysis, we included a swath profile for the rainfall data and the mean ksn. Based on the swath profiles described below, and after grouping the AFT data according to their spatial distribution, we discriminated six subregions (SEC2W, SEC2E, SEC3C, SEC4W, SEC4C, and SEC4E) to perform the statistical analysis. In doing so, the main objective was to obtain significant results for areas with an acceptable density of thermochronological data. Finally, a color bar representing the main geological units was included on each swath in order to detect a possible interplay between erAFT and lithological changes.

A first general view of the spatial variability of the thermochronological, topographic and climatic data is shown in Figure 4. In terms of exhumation/erosion, the youngest cooling ages, spanning from the Miocene to the Pleistocene, were identified in subzones SEC2W and SEC2E, which also show moderate to high erosion rates (erAFT) with a median of 0.99 km/Myr and 2.24 km/Myr, respectively (Figs. 4A, B). Subzone SEC2E stands out because it also shows the highest local relief (2695 m, Fig. 4C), HI (0.68, Fig. 4D), ksn (419, Fig. 4E), and rainfall rates (3795 mm/yr, Fig. 4F). The 5 km-radius relief distribution (Fig. 4C) reasonably mimics the ksn distribution (Fig. 4E), showing higher values on the eastern foothills, for example a median of 1567 m in SEC4E, and lower values in the axial and western subzones with median values below 1000 m. The HI index analysis (Fig. 4D) indicates that the erosional state of most subzones corresponds to an equilibrated landscape with a median ranging from 0.32 (SEC4E) to 0.45 (SEC2E). Outliers above 0.5 were recovered for subzones SEC4W and SEC4C, with the HI distribution for subzones SEC2W, SEC2E and SEC3C also surpassing this value, suggesting that some areas experienced recent landscape rejuvenation. Annual rainfall strongly fluctuates across the EC, with rainfall higher in the eastern foothills (e.g., SEC2E and SEC4E) and lower in the central axial domain (e.g., subzone SEC4C, Fig. 4F).

Figure 4. Variability of the compiled thermochronological data (A. AFT; B. erAFT), the measured topographic metrics (C. local relief; D. HI; E. ksn), and (F.) the mean annual rainfall for each analyzed subregion. Each box was colored according to its location in the swath profiles described below. Greyish boxes correspond to subregions in swath SEC2 (SEC2W and SEC2E). The yellow-colored box corresponds to subzone SEC3C and the blue-colored boxes correspond to the subregions in swath SEC4 (SEC4W, SEC4C, and SEC4E). Please refer to Figure 3 for the spatial extent of each box.

Along profile SEC1, we observed two areas with contrasting topography and high values of all the studied metrics. The western area is located on the La Yuca Fault (western foothills), where an increase in local relief and ksn (up to ~160) is visible. The eastern area lies between the Río Blanco and the Algeciras Faults, where basement rocks are already exposed at the surface. Structurally, this area resembles a large asymmetrical positive flower structure of the Algeciras Fault. This faulted block has a width of ~ 4 km and shows the highest elevations (>3200 m) and relief (> 1800 m), and THi* values above 0.5 (Fig. 5). The ksn value peaks in this area, rapidly increasing east of the Pandi Fault up to 300. Also there, Late Miocene – Pliocene (5.5 to 3.5 Ma) apatite (U-Th)/He ages were recently reported by Pérez-Consuegra et al. (2021), evidencing exhumation rates as high as 1.7 km/Myr. Another smaller peak in the ksn index between the Algeciras and Ucrania faults corresponds to the highest rainfall rates. In this region, a rainfall peak of ~4415 mm/yr was observed at a distance of ~14 km from the eastern mountain front bounded by the Algeciras Fault, correlating with a mean elevation of 1770 m and a 5 km-radius relief of 1150 m (Fig. 5). In contrast, the western foothills show a peak rainfall of ~3260 mm/year, i.e., 35% lower than on the eastern side. We attribute the high topographic metrics to a juvenile landscape where tectonic deformation is weakly coupled with rainfall. The presence of deep V-shaped valleys and hanging knickpoints are potentially correlated with a rapid incision of the Duda River to compensate for the uplift event.

Figure 5. Swath profile SEC1, condensing topographic and climatic data in the southern EC. (A) Plot showing the minimum, mean, and maximum elevation profiles and published single grain apatite (U-Th)/He ages (AHe) (Diamond markers; Pérez-Consuegra et al., 2021). The color bar at the bottom of the swath represents the main geological units presented in Figure 1B. (B) Local relief and THi* indexes. (C) Mean ksn profile. (D) Minimum, mean and maximum Mean Annual Rainfall (MAR). The field photographs below (E, F) show the deep V-shaped valley of the Duda

River (looking downstream) and hanging valleys with vertical knickpoints in the area where high relief and ksn patterns are observed. The approximate location of the photos is shown by the red circle in panel A. Please refer to Figure 1A for details of the swath location.

Along profile SEC2, we identified two subregions with good coverage of AFT data (SEC2W and SEC2E, Fig. 6). Subregion SEC2W is located between the edge of the axial plateau at an elevation above 2600 m and the Middle Magdalena Valley. The subregion includes four structures, of which the Alto del Trigo and Bituima Faults are the most important. It is precisely between these two structures that we find moderately high erAFT ranging between 1 and 2 km/Myr, correlating with 5 km-radius relief values above 600 m, ksn below 150 and rainfall rates of 1800 to 2000 mm/yr.

An interesting inverted cooling path is observed in this region, with younger AFT ages (1.9 Ma; Guerrero, 2018) at higher elevations (~ 2800 m; Fig 6), separated from Miocene AFT ages by the Bituima and Alban Faults, which could be responsible for this variation. On the other hand, the SEC2E subregion corresponds to rapid erosion rates up to 3 km/Myr, the highest in the EC. A rapid exhumation zone concentrated between the Servitá and Bogotá Faults is responsible for these Pliocene to Pleistocene AFT cooling ages (Fig. 6). Furthermore, the presence of totally annealed ZFT cooling ages (Parra et al., 2009a) reveals the post-Early Miocene (ca. ~18 Ma) exhumation of lower crustal levels of the Quetame Massif. At higher elevations, erAFT values decrease to less than 1 km/Myr, passing to un-reset ages in the axial plateau. Despite the lithological contrasts between the two flanks, rapid erosion rates were detected in both areas.

The Quetame Massif corresponds to the Mora et al. (2008) study area, where these authors proposed a climate-driven denudation model for the EC. A rainfall peak of 4370 mm/yr was obtained at a distance of ~16 km from the mountain front, correlating with a mean elevation of 1772 m and a 5 km-radius relief of 1700 m (Fig. 6). Conversely, the western foothills display a peak rainfall of 2260 mm/yr. As shown in Figure 6, there is a spatial match between high MAR values (above 4000 mm), high ksn (above 300), high LR (>2000 m), and moderately high THi* values. However, some high values of the ksn index (> 200) extend inward over the upper slopes where rainfall rapidly decreases to less than 1500 mm/yr.

Figure 6. Swath profile SEC2, condensing topographic, thermochronological and climatic data in the central-southern EC. (A) Plot showing the minimum, mean, and maximum elevation profiles and the compiled AFT data. The color bar at the bottom of the swath represents the main geological

units presented in Figure 1B. (B) Long-term erosion rates (erAFT) derived from the AFT data are shown in panel A. (C) Distance-age relationship for swath SEC1; the zircon (U-Th)/He (ZHe) and AHe data represent the average of a group of ages according to Moreno et al. (2013). (D) Local relief and THi* indexes. (E) Mean ksn profile. (F) Minimum, mean and maximum Mean Annual Rainfall (MAR). Please refer to Figure 1A for details of the swath location.

Along profile SEC3, only one area with sufficient AFT data (SEC3C, Fig. 7) was identified. This subregion was identified on the uppermost eastern slope associated with the Guayabal Fault, where Cretaceous and Cenozoic sedimentary rocks crop out. In the footwall of this fault, we compiled AFT data recording Eocene - Miocene partially annealed ages. Immediately to the east, fully annealed AFT and AHe ages have been reported from the hanging wall of the Guayabal Fault (Parra et al., 2009b; Ramirez-Arias et al., 2012), representing a Miocene exhumation event with moderate erAFT values (0.7 and 0.9 km/Myr). In this area we also noted a rapid increase in topography (> 3000m), local relief (~1800 m) and ksn (>200), suggesting a likely coupling between erAFT and topographic metrics. For this swath, on the eastern foothills rainfall peaked at a distance of 29 km from the mountain front bounded by the Guaicaramo Fault. This rainfall peak of 3810 mm/year is associated with a mean elevation of 1140 m and a 5 km-radius relief of 700 m. Contrary to the rainfall trends observed in swaths SEC1 and SEC2, the western foothills of the EC at this latitude receive more rainfall than the eastern foothills. A rainfall peak of ~4300 mm/yr was observed on the lowermost slopes of the western side. Remarkably, the highest rainfall rates recorded across the range on both foothills are not well correlated with Andean cooling events but with pre-Andean events, i.e., Oligocene in age on the western side and Eocene – Lower Miocene on the eastern side (Fig. 7). Although AFT data are scarce on both foothills, the spatial relationship between long-term exhumation and short-term rainfall is negligible.

Figure 7. Swath profile SEC3, condensing topographic, thermochronological and climatic data in the central EC. (A) Plot showing the minimum, mean, and maximum elevation profiles and the compiled AFT data. The color bar at the bottom of the swath represents the main geological units presented in Figure 1B. (B) Long-term erosion rates (erAFT) derived from the AFT data are shown in panel A. (C) Distance-age relationship for swath SEC1; the AHe data represent the average of a group of ages according to Ramírez-Arias et al. (2012). (D) Local relief and THi* indexes. (E)

Mean ksn profile. (F) Minimum, mean and maximum Mean Annual Rainfall (MAR). Please refer to Figure 1A for details of the swath location.

Profile SEC4 represents the ideal scenario to test the climate-driven hypothesis, considering the large amount of available thermochronological data (Fig. 8). For this swath, we classified three subregions from west to east as SEC4W, SEC4C, and SEC4E. Along this swath, Ramírez-Arias et al. (2012) supported previous interpretations and reinforced the climate hypothesis proposed by Mora et al. (2008). Subregion SEC4W is characterized by moderate topographic hills reaching a maximum elevation of around 1900 m. Partially annealed ages (middle Eocene–early Oligocene) over the hanging wall of the La Salina Fault system are associated with initial thrusting along this structure, followed by an early middle Miocene exhumation event (Mora et al., 2010a; Sánchez et al., 2012). Low-angle thrusting into the MMV exposed Cenozoic (Paleogene) strata in this area. These data allow us to compute low to moderate erAFT between 0.5 and 1.1 km/Myr. In contrast, un-reset ages are observed in the footwall of the La Salina Fault system. We also obtained relief values below 1200 m and low ksn (< 100) in this area, but high rainfall rates. As in swath SEC3, the western foothills are more humid than the eastern foothills, showing a 4626 mm/yr rainfall peak (Fig. 8). At first glance, high rainfall rates do not necessarily imply high erAFT as in subregion SEC2E (Fig. 6).

The central segment classified as SEC4C is interesting, as some authors have stated that the inverted Boyacá Fault has been a relevant structure for pre-Andean (Early Eocene to Early Oligocene) exhumation events (Parra et al., 2009a; Mora et al., 2010a; Ramírez-Arias et al., 2012; Saylor et al., 2012a; Silva et al., 2013; Reyes-Harker et al., 2015). Between the Boyacá and the Soapaga Faults, we observed the Floresta Massif (Paleozoic rocks) with ZHe ages of ~33.8 Ma (Saylor et al., 2012a), representing the onset of exhumation in a Pre-Andean phase. In contrast, the presence of totally annealed Miocene cooling ages suggests ongoing exhumation in the Eastern Cordillera hinterland (Fig. 8). Erosion rates in this subregion are low, mainly below 0.8 km/Myr independent of the faulted block and the lithology. A peak in relief (above 1500 m), THi* (>0.5) and ksn (200 – 240) spatially correlates with the highest elevations and the hanging wall of the Boyacá Fault. However, these values rapidly decrease on the footwall of the Boyacá Fault, that is, in turn, the hanging wall of the Soapaga Fault. This may indicate active surface uplift restricted to the Boyacá Fault.

Finally, subregion SEC4E corresponds to the eastern foothills where the topography rapidly decreases from more than 3000 m elevations to less than 500 m in the Llanos Basin, east of the Yopal Fault (Fig. 8). AFT data compiled here evidence how reactivated reverse faults, such as the Pajarito and Guaicaramo Faults, were responsible for controlling two pulses of exhumation (Late Oligocene – Early Miocene and Late Miocene, respectively) of the cordillera (Ramírez-Arias et al., 2012). Visually, this is easy to recognize as Cenozoic un-reset ages are restricted to the footwall (Guaicaramo Fault), whereas fully annealed Cretaceous samples on the hanging wall disclose a moderate Miocene exhumation event with erAFT up to 1 km/Myr. This subregion correlates with local relief ranging between 600 and 1200 m, high ksn values (>200) and moderate to high rainfall rates. In the eastern foothills, a rainfall peak was observed at a distance of 19 km from the mountain front bounded by the Yopal Fault. These 4040 mm/yr rainfall peaks are correlated with a mean elevation of 1250 m and a 5 km-radius relief of 900 m. Similar to subregion SEC2E (Fig. 5), the ksn peak is slightly displaced to the west of the rainfall peak, and fully annealed apatite samples are found on higher elevations where rainfall rapidly decreases to less than 2000 mm/yr (Fig. 8).

Figure 8. Swath profile SEC4, condensing topographic, thermochronological and climatic data in the northern EC. (A) Plot showing the minimum, mean, and maximum elevation profiles and the compiled AFT data. The color bar at the bottom of the swath represents the main geological units presented in Figure 1B. (B) Long-term erosion rates (erAFT) derived from the AFT data are shown in panel A. (C) Distance-age relationship for swath SEC1; the ZHe and AHe data represent the average of a group of ages according to Ramirez-Arias et al. (2012), Sánchez et al. (2012), Saylor et al. (2012a) and Reyes-Harker et al. (2015). (D) Local relief and THi* indexes. (E) Mean ksn profile. (F) Minimum, mean and maximum Mean Annual Rainfall (MAR). Please refer to Figure 1A for details of the swath location.

6.2 Seismic parameters: Strain rates, energy, and uplift

We calculated these seismic metrics along the six subzones inside the previously described swath profiles. In order to compare significant differences in the estimated values of *a* and *b* from the Gutenberg-Richter (magnitude-frequency) relationship, the EC was partitioned using an algorithm considering latitude and longitude, splitting the area into 4^n with (n=1,...,3); that is, first into four quadrants, then into 16 quadrants, and so on, always satisfying the imposed condition that there were at least 20 earthquakes in the area (Bermúdez et al., 2013). After these partitions were made

on each subarea, the values of *a* and *b* were calculated. For this reason, we show all the seismic values calculated for those subdivisions: SSR4, SSR16 for seismic strain rates, SE4, SE16 for seismic energy, and u4, u16 for seismic uplift, respectively (Fig. 9 and Supplementary Figure S3). The difference between the division into 4 quadrants and 16 quadrants is that the first is influenced by more regional patterns, whereas local structures may influence the second.

The highest values of average seismic strain rate (SSR4) were recorded in subzones SEC2E (7.90E-16 s^{-1}), SEC4E (2.95E-16 s^{-1}), SEC3C (2.82E-16 s^{-1}), and SEC2W (1.15E-16 s^{-1}; Supplementary Fig. S3). The zones SEC2W (1.15E-16 s^{-1}) and SEC2E (7.90E-16 s^{-1}) have contrasting average SSR4 values. When downscaling, subregions SEC2E (3.61E-16 s^{-1}), and SEC3C (3.40E-16 s^{-1}) exhibit the highest average SSR16 values (Fig. 9), although in general terms seismic deformation tends to decrease in all regions. These sectors also experienced high average seismic rock uplift u16 (952.62, 709.24 meters, respectively), during the last 5 Ma. Similarly, SEC4E shows a significant average seismic uplift (u4 = 635.60 m), but this estimate decreases as the scale is reduced. In contrast, subregion SEC2E shows a two-fold increase in the seismic uplift rate correlated with the seismic swarm west of the Servitá Fault (Fig. 2). There, the u16 distribution shows an interquartile range between 0.5 and 1.5 km. The highest values of average seismic energy (SE4) are observed in SEC2E (6823493.10 J) and SEC4W (7564530.71 J). However, when the observing the 16-quadrant results, the average SE16 values decrease in regions SEC2E (3094907.00 J), SEC3C (76498.66 J) and SEC4W (3410070.79 J), but increase in regions SEC2W (2028661.54 J), SEC4C (1973960.89 J) and SEC4E (1104556.83 J).

Figure 9. Seismic metrics for the Eastern Cordillera of Colombia after partitioning the study area into 16 quadrants. (A) Seismic Strain Rate; (B) Seismic Energy; (C) Seismic Uplift. The variability of each seismic metric is presented as boxplots (D, E, and F). Please refer to the main text for further details.

6.3 Statistical analysis: Pearsonian correlation and ANOVA tests

In order to analyze the spatial correlation between potential forcing parameters, we show the Pearsonian correlogram in Figure 10. The white spaces indicate either no correlation between variables or that the values for each pixel are constant, which is why the calculated standard deviation is zero, and it is not possible to calculate correlations. To facilitate the integration of our results in discriminating possible controlling processes (climate, tectonics or relief) on long-term

exhumation rates, we focus the spatial correlation on subzones SEC2W, SEC2E, SEC3C, SEC4W, SEC4C (Fig. 3), described above. Note that the extent of each subzone in Figure 3 is, in some cases (SEC2E and SEC4C), larger than the swaths. This is because the earthquake data are not homogeneously distributed and do not necessarily match the areas sampled for thermochronological analysis. Thus, we are compelled to consider seismicity in a broader swath environment, so as to improve estimates of *a* and *b*-values and obtain values that are statistically representative.

We emphasize testing the spatial correlations between the long-term exhumation rates in the EC derived from AFT thermochronology and erCN. Given that we compare all variables for six areas, correlations are statistically significant (at a 90% confidence level) for a Pearson correlation coefficient $r \geq 0.6$. When all the analyzed subregions are included on the same regression, local relief (LR) shows a positive correlation with SSR4 (r = 0.6), u4 (r = 0.6), and ksn (r = 0.8). When including the erCN with all the subregions, erCN only correlates with erAFT (r = 0.6). In contrast, erAFT displays a spatial match with LR (r = 0.7) and seismic parameters such as SSR4 (r = 0.8) and u4 (r = 0.8). In this first regional approach, short-term rainfall rates (R) show a weak spatial connection with erAFT and erCN (Figs. 10A and 10B).

Figure 10. Pearsonian correlation coefficients between erAFT, erCN and the studied metrics. Given that we compare all variables for six areas, correlations are statistically significant (at a 90% confidence level) for a Pearson correlation coefficient $r \geq 0.6$.

The thermal history of the EC is spatially variable across geological time, thus the erosion rates and topographic development can increase or decrease in different periods as a result of the interaction of different processes (e.g., climate or tectonics). We therefore performed a Pearson correlation analysis in order to distinguish if there exists any controlling mechanism for each of the six studied subzones (Figs. 10C to 10H). Figure 10C for subzone SEC2W shows a significant negative correlation (r = -0.7) between SSR16 and erAFT, whereas there is a lack of correlation with rainfall rates (r = 0.01). In contrast, for subregion SEC2E (Fig. 10D), the most significant correlations are: erAFT versus seismic parameters (SSR4, u4, SSR16, and u16; r > 0.7), LR (r = 0.6), and rainfall (r = 0.6). Rainfall rates also correlate significantly with erCN (r = 0.7). Despite this positive correlation, we observed a decoupling between average erAFT (2.36 km/Myr) and erCN (0.226 km/Myr) in SEC2E, accounting for a ten-fold increase in long-term denudation rates.

For the SEC3C zone (Fig. 10E), erosion rates derived from cosmogenic isotopes (erCN) correlate significantly with erAFT (r = 0.6), ksn (r = 0.7), LR (r = 0.7), and all the seismic indexes ($r \geq 0.8$) with seismic strain rate (SSR) and seismic uplift (u) evidencing the strongest correlations (r = 0.9). In contrast, erAFT displays weak correlations with all the potential controlling factors, with the highest corresponding to those matched with SSR and u (r = 0.5). The topographic relief, which is subdued in the axial plateau (Supplementary Figure S2), correlates with all the seismic metrics, with coefficients $r \geq 0.6$.

For the SEC4W sector, no significant positive correlations were observed between erosion rates derived from cosmogenic isotopes (erCN) or derived from AFT ages (erAFT) with seismic or climatic parameters. In contrast, erCN rates correlate negatively with seismic energy SE4 or SE16 (r = -0.6), with seismic strain rate (SSR16, r = -0.7) and seismic uplift (u16, r = -0.7). The erAFT correlate weakly with SSR4, and u4 (r = 0.3). HI, which is related to the erosional state of the landscape, correlates positively with SSR4 (r =0.7), u4 (r =0.7), SSR16 (r =0.9) and u16 (r =0.9). In addition, ksn correlates with local relief (LR, r = 0.8), SE4 and SE16 (r = 0.6), ssr16 (r = 0.7) and u16 (r = 0.7). Local relief for this sector correlates with long-term seismic measurements SSR4, u4, SSR16, and u16 (r > 0.5) (Fig. 10F).

Similarly, for the SEC4C subregion (Fig. 10G), the fact that the seismic strain rates are constant in each pixel prevents the study of correlations with erAFT, however, we observe significant correlations between LR and ksn (r = 1.0), LR vs HI (r = 0.6), and LR vs seismic uplift u4, and u16 (r = 0.6). There is no correlation between rainfall and LR or rainfall and erAFT. For the SEC4E zone (Fig. 10H), no spatial correlation was observed between seismic measurements and erAFT, nor between erAFT and LR. No correlation was found between these last two variables and rainfall either. A moderate correlation (r = 0.5) was observed between HI versus SSR16 and u16 (r = 0.6). The ksn, an erosion proxy index, correlates with SE4 (r = 0.7) and SSR16 (r = 0.6). It is noteworthy that ksn weakly correlates with LR and that HI correlates weakly and negatively with LR (r = -0.6).

Figure 11. Relationships between erosion rates (both erAFT and erCN) and predictors. The statistical analysis considers only uninterpolated data for each studied subregion (SEC2W, SEC2E, SEC3C, SEC4W, SEC4C, and SEC4E).

The second statistical analysis allowed us to achieve greater discrimination of the potential forcing parameters controlling long-term erosion rates. The results are shown as lolliplots (Fig. 11), where

the *x*-axis represents the standardized coefficient and the *y*-axis represents the predictors or independent variables. The blue or red colors indicate each variable's positive or negative effects, respectively, either on erAFT or erCN data. In global terms, for uninterpolated data and including subregions with erCN and erAFT (Figs 11A, 11B and 11C), we observed a significant tectonic control, which is inferred from the influence of seismic strain rate (SSR4) and seismic energy (SE4) over short-term erosion rates (erCN) and long-term exhumation (erAFT). For erCN, the seismic energy (SE4) is the best positive predictor variable (1.4), while rainfall patterns have a limited influence (0.092). Our long-term erosional proxy, erAFT, is positively influenced by SSR4 (0.61), and to a lesser extent by LR (0.4); in contrast, the effect of rainfall (R) rates is not significant (r = 0.043; Fig. 11B).

When downscaling this analysis to each subregion, new trends emerge. In Figure 12, we present a block diagram with the best-correlated predictors for each subregion. A detailed analysis of each area suggests that on five (SEC2W, SEC2E, SEC3C, SEC4W, and SEC4E) of the six analyzed areas, tectonic-related parameters such as SSR16 or SSR4 represent the best predictor variables of erAFT (Figs 11D, 11F, 11G, 11H, 11I, 11J and 11L). Whereas the climate proxy positively influences erosion rates for SEC2E (erCN = 1.2 and erAFT = 0.63), the significant difference in erAFT and erCN restricts our interpretation of climate as a primary driver, at least in the long term. In subregions, SEC4C and SEC4E, the short-term erosion proxy, the ksn index, is negatively correlated with erAFT (Fig. 12). One hypothesis could be related to non-consolidated sedimentary cover on reaches where sediment flux surpasses water discharge, forcing transport-limited behavior.

Figure 12. Schematic block model for the EC, showing the spatial distribution of each analyzed subregion and the best predictor variable (considering only standardized coefficients > 0.6) either for erCN (dashed arrow) and/or erAFT (solid arrow). The length of each arrow was scaled, considering a standardized coefficient of 1.0. SSR = Seismic Strain Rate; SE = Seismic Energy; LR = Local Relief.

6.4 Estimation of surface uplift in the Quetame Massif

In general, we observe an average net surface uplift between 1.4 and 1.8 km for this part of the orogen (Fig. 13). The net uplift seems to increase towards the northern catchments, reaching up to ~1.9 km (considering the upper bound). A remarkable pattern of convex reaches is visible in some streams, denoting major knickzones bounding the erosional wave migrating upstream or, more

recently, localized surface uplift forced by faulting (e.g., the Servitá Fault). This pattern could be analyzed in the Guatiquía River profile (Fig. 13E). The ksn pattern depicted for this catchment resembles the expected pattern for an incisional wave, with higher ksn values observed in the main trunk (e.g., Wobus et al., 2006), whereas tributaries show medium to low values. However, this pattern seems to correspond to at least two different uplift events, which may explain the broad two convex reaches observed (Fig. 13D). A first event may have led to a surface uplift of ~ 1000 m, whereas a later event may have induced additional uplift of ~715 m. Additional constraints such as strath terraces dating or paleoelevation estimations are needed to confirm or refute this interpretation.

7. Discussion

7.1 Linking exhumation/erosion rates with potential forcing parameters: climate or tectonics?

Whether long-term exhumation/erosion rates in mountain belts are controlled to a first order by climate or tectonic processes remains debatable. In the EC case, some authors have suggested that climate forcing has been acting coevally with rock uplift since the Late Miocene and even in Pliocene-Quaternary times (Mora et al., 2008, 2013, 2015; Ramirez-Arias et al., 2012). Those authors have based their proposal of climatic forcing on AFT data, published palaeobotany studies identifying that a wetter climate in the vicinity of the Amazon basin had already developed in Miocene times (Hoorn 1994; van der Hammen and Hooghiemstra 2000; Kaandorp et al. 2005; Hoorn et al., 2010), and short-term rainfall data. In contrast, in the Merida Andes, which are contiguous to the EC, a robust tectonic control on long-term erosion rates has been presented (Bermúdez et al., 2013). Based on the remaining uncertainty for the Colombian EC, we raise the following questions. Can the arguments of Mora et al. (2008) be extrapolated to the entire EC? More broadly, how strongly are tectonic and climatic processes coupled, and on what time scales?

A first interpretation of the role of short-term rainfall on denudation rates supports our hypothesis that tectonics rather than climate represent the primary conditioning factor in the EC. As demonstrated in Figure 6, the highest MAR overlaps with the rapid erosion rates (> 2 km/Myr) computed on the hanging wall of the Servitá Fault, but rapidly decreases as the topography increases and relief decreases. This rainfall peak (4370 mm/yr) is located to the east of a region with a 5 km-radius relief of 1.7 km and moderate elevation (mean ~1.7 km). These values agree with the threshold relief expected to enhance heavy orographic rainfall (Bookhagen and Strecker, 2008). We therefore argue that the climate-driven model proposed for SEC2E better reflects a partial spatial

correlation observed due to a relief-driven rainfall distribution that is not fully coupled with the long-term erosion rates derived from the AFT data reported by Mora et al. (2008, 2010b). Further evidence against the climate-driven model could be derived from the regional pattern of exhumation/erosion rates and short-term rainfall rates north of latitude 5°N. As observed in Figures 6, 7 and 8, high rainfall rates do not necessarily imply high erAFT rates. Subzones SEC2E, SEC4W and SEC4E receive a very similar amount of rainfall (4370, 4626, and 4040 mm/yr, respectively), however erAFTs are two to three times higher in SEC2E. These qualitative observations also undermine the notion that the topographic asymmetry of the range results from accelerated exhumation rates in a climate-driven model (Mora et al., 2008). Even though the EC's western foothills are more humid in swaths SEC3 and SEC4 than the eastern foothills, the asymmetry remains equal, i.e., with the eastern foothills being steeper and shorter than the western ones. Thus, an alternative mechanism rather than the climate needs to be evaluated to explain the diachronous exhumation and topographic development of the range. In section 7.3 below, we attempt to provide a feasible explanation considering a "tectonic" driver.

Our statistical approach considering erosion rates (erAFT and erCN) and potential controlling factors (climatic, topographic and seismic factors) seeks to avoid subjectivity in testing the potential spatial correlation, and reveals a complex system where the interaction between these parameters is intricate. The pattern of seismic parameters (e.g., SSR16) correlating spatially either with erAFT (e.g., subzones SEC2W, SEC4W, and SEC4E, Fig. 12) or with erCN (e.g., subzone SEC3C) could lead us to interpret a potential link between tectonics and erosion rates in the EC. In subzone SEC4E, despite several authors having demonstrated how deformation is actively migrating towards the Llanos Basin (e.g., Veloza et al., 2015), SSR16 is a good predictor of erAFT in the mountainous area (Fig. 12). This may indicate that some recent surface uplift has occurred in subregion SEC4E, whereas the deformation front along the Yopal Fault continues to advance forelandward (e.g., Bande et al., 2012). We therefore propose that long-term exhumation/erosion has been coupled to active faulting through coseismic deformation in the past 5 Ma. These results agree with the rapid erosion rates computed for tectonically active areas with potentially active structures such as the Servitá Fault (Fig. 6). In other regions (e.g., SEC4C, Fig. 12) the poor correlation with the seismic parameters and erosion rates argues against active tectonic deformation or aseismic deformation (e.g., Vernon et al., 2009).

Figure 13. Projected profiles for selected catchments that drain the páramos of Sumapaz and Chingaza. NaF = Naranjal Fault; SvF = Servitá Fault. The top-right figure shows the ksn pattern for

the Guatiquía River and the analysed low-relief landform. The bottom-right figure for the same catchment shows an oblique Google Earth image with the net surface uplift inferred for the Páramo de Chingaza. Note how the erosional wave migrating upstream through the Guatiquía River, evidenced by the typical ksn pattern, has resulted in a highly incised landscape. The yellow markers correspond to major knickpoints. The uppermost knickpoint used to project the river profile is shown as a red marker.

The persistent weak correlation between rainfall rates and erAFT and erCN suggests a poor control of climate on erosion rates. Only in subzone SEC2E, which matches the study area of Mora et al. (2008), were significant correlations between rainfall and erCN observed (Fig. 12). Hernández-Chaparro et al. (2021), using a 3D thermokinematic model for the Guayuriba catchment in part of subzone SEC2E, emphasized the correlation between rainfall rates, erAFT and erCN. When considering only tectonic blocks delimited by the Quetame, Naranjal, Quebrada Grande and Servitá faults, these authors observed that seismic parameters are better predictors for the present-day relief. Despite this, we computed a ten-fold increase in erAFT compared to erCN. These differences could be related to geomorphological factors such as changes in river dynamics, sediment supply, etc. Since the fluvial system responds to changes in boundary conditions relatively rapidly to achieve steadiness (0.25 to 2.5 Ma, Whipple, 2001), a geomorphological process might explain the decoupling between erAFT and erCN. Based on analytical solutions and numerical simulations, Baldwin et al. (2003) demonstrated how several processes, such as a transition from detachment- to transport-limited conditions and isostatic rebound, have the potential to delay the fluvial response by a factor of 3 to 6, respectively. The transition from detachment- to transport-limited models is favorable when vast amounts of coarse sediment are delivered to the river valleys, for example, after earthquakes, causing sedimentation and negative mass balances, thus reducing the river response to external forcing (e.g., Korup, 2006; Ouimet et al., 2007). Considering the seismo-tectonic setting and high rainfall rates of the area (Figs. 2 and 3) and the strong correlation between erAFT and seismic predictors (Fig. 12), both runoff and earthquakes have the potential to enhance long-term sediment supply into the river system. This hypothesis may explain the persistence of the transient state in this subregion despite high rainfall rates.

Finally, we also tested the potential role of lithology in controlling exhumation rates in the EC. Braun et al. (2014) proposed that rock density variations could control surface lowering rates in igneous-metamorphic massifs. The rationale behind this concept is that the exhumation of dense

rocks (e.g., metamorphic rocks) is faster when they are in contact with lighter rocks (e.g., sedimentary rocks), potentially triggering an isostatic uplift capable of creating new topographic relief. Within the Quetame Massif, the highest identified erAFTs were partially associated with low-grade metasedimentary rocks cropping out in faulted contact with Paleozoic and Cretaceous sedimentary rocks. The AFT data distribution reveals similar cooling ages independent of the lithology (by comparison between Figs. 1B and 3). Indeed, the youngest ages (0.8±0.3 and 0.9±0.2, Mora et al., 2010a) were obtained from Paleozoic sandstones on the Servitá Fault hanging wall.

Furthermore, Saylor et al. (2012b) sampled basement (granitoids and gneisses) and sedimentary rocks (Jurassic, Paleozoic and Paleogene in age) of the Floresta Massif for thermochronological analysis (U-Th/He in zircon). These samples gave similar patterns as those observed in the Quetame Massif, limiting the role of lithology on exhumation rates. For instance, the younger average cooling ages of 24.6±2.6 Ma (n=16) and 24.9±3.9 Ma (n=4) were obtained from the basement and Jurassic sedimentary rocks. Basement rocks cropping out on the Soapaga Fault hanging wall also record older ages (e.g., 30.3±1.9 Ma, n=11). These observations argue against the role of rock type in promoting faster exhumation rates in the Colombian EC. What has been observed is that including lithological variations and bootstrapping techniques is optimal to estimate erosion rates in transient landscapes modelled using 3D thermokinematic methods, as demonstrated recently in the northern EC by Bermúdez et al. (2021).

7.2 How strongly were climate and long-term exhumation rates coupled in the late Cenozoic history of the EC?

As the rainfall distribution observed in the EC at the present time was probably established from the Holocene (van der Hammen and Cleef, 1992), the long-term climate influence on the exhumation and landscape evolution cannot be studied with the TRMM data used in section 7.1. Despite the poor correlation shown above between short-term rainfall and erAFT, additional sedimentological, thermochronological, and geomorphological evidence is required to provide reliable analyses.

Considering long-term coupling, climate-tectonic interactions can be analyzed using three models (Whipple, 2009): (i) the fixed-width system, (ii) the frictional critical-taper wedge, and (iii) the hot orogenic system (the latter is not considered in this work, see Whipple, 2009 for further details). The fixed-width system is well known for establishing that under an increase in erosional efficiency (assumed to be equal to high rainfall patterns and high erosion rates), erosional unloading will induce a passive isostatic rebound, followed by an increase in sediment delivery to surrounding

depositional basins. Accordingly, topographic asymmetry is induced by a reduction in erosional efficiency under a steady-state landscape (Bonnet and Crave, 2003). However, when tectonic uplift is ongoing, the transient landscape must adjust, and erosional efficiency will induce an isostatic uplift (Whipple, 2009). The fixed-width model has been demonstrated in tectonically inactive mountains or with isostatic rebounds associated with deglaciations (e.g., the European Alps, Cederbom et al. 2004; Champagnac et al. 2007). This model fits with the EC hypothesis (Mora et al., 2008, 2013, 2015). The shortcoming here is that this model has the inconvenience that it assumes a regional simple block-uplift pattern, which is not the case in the EC (Fig. 3).

The second mechanism described by Whipple (2009) is associated with a frictional critical-taper wedge, a model proposed for the EC (e.g., Mora et al., 2008; Parra et al., 2009a; Ramirez-Arias et al., 2012). In this model, several criteria can be used to better assess if there is a climate influence on tectonic processes:

The retreat of active deformation to the interior of the range with the further acceleration of active shortening: Some authors have presented shortening rates along the eastern foothills showing a decrease rather than an increase since Miocene times, evolving from 5 mm/yr (Mora et al., 2008) to only 2.1 mm/yr measured along the Tame Fault (Veloza et al., 2015). In addition, geomorphic, sedimentologic and detrital thermochronology evidence suggests almost continuous forelandward migration of the deformation front from the Oligocene until the present (Audemard, 1999; Mora et al., 2010b; Bande et al., 2012; Veloza et al., 2015), which is opposite to what would be expected in a climate-driven model (Whipple, 2009).

Increase in sedimentation adjacent to the deformation front: For the eastern foothills of the EC, several authors (e.g. Ramirez-Arias et al., 2010, 2012) have shown that since Miocene times, syntectonic sedimentation has increased. For instance, at the Nunchia Syncline on the footwall of the Guaicaramo Fault, more than 2 km of syntectonic orogenic detritus with an Andean signature were deposited (Bande et al., 2012). Assuming that the Late Miocene rainfall pattern on the Andean foothills had similarities with the present-day climate (e.g., Kandorp et al., 2005; Anderson et al., 2015), we could reason that there is a positive correlation between rainfall and the amount of sediment evacuated from the orogen towards the Llanos foreland basin.

Reduction of foreland subsidence: Since the middle-late Eocene uplift episodes of the EC (Parra et al., 2009a; Mora et al., 2010a; Saylor et al., 2012b; Siravo et al., 2018), the tectonic loading prompted flexural subsidence on both flanks of the Eastern Cordillera (Bayona et al., 2008; Ramírez-Arias et al., 2010; Delgado et al., 2012; Mora et al., 2019), the opposite to the expected in

a climate-driven model. For instance, the ~3 km pile of syntectonic detritus produced by the tectonic inversion of the Pajarito – Guaicaramo faults were stored on a subsidizing foreland. Mora et al. (2010b) interpreted the ~3 km thick Corneta Formation, on the footwall of the Guaicaramo thrust, as evidence of accelerated subsidence after 5 Ma.

The decrease in relief: Contrary to expectations, we obtained values of LR up to 2900 m, especially along the Servitá Fault (subregion SEC2E, Fig. 6). Along the strike of the eastern foothills of the EC, where the rainfall pattern is high, LR shows medium to high values. Thus, we do not observe the expected subdued topography resulting from the increase in denudational processes and low tectonic activity.

Based on what would be expected for a climatic forcing in a critical-taper wedge system (Whipple, 2009), most of the requirements are undoubtedly unsatisfied. Thus, the hypothesis that climate has been acting as a primary control on mountain building along the EC of the Northern Andes is challenging to maintain. We have demonstrated that climate is a potential controlling factor only in the Quetame massif area and extrapolating this positive feedback to the whole range is unfounded. These findings support a dominance of tectonic activity over climate as the primary driver of exhumation, erosional patterns and topographic growth of the Colombian (Struth et al., 2016; Siravo et al., 2018), Venezuelan (Bermúdez et al., 2013), Bolivian (Whipple and Gasparini, 2014), and central (Hoke et al., 2007) Andes mountains. Our work also casts doubt on the recently proposed worldwide acceleration in erosion rates during the Plio-Pleistocene (e.g., Herman et al., 2013; Willett et al., 2020).

7.3 What mechanism drove exhumation/erosion of the Eastern Cordillera in the late Cenozoic?

As we have shown above, there is a good regional agreement between the exhumation patterns and tectonic variables for most of the studied subregions (Fig. 12). Nevertheless, a key question remains unanswered: how to explain the along-strike changes in the long- to short-term exhumation and denudation rates of the EC? The late Cenozoic tectonic evolution of the Northern Andes has been a controversial matter of debate. Several models have been invoked to explain the present-day instrumental seismicity and stress pattern associated with plate reorganization (e.g., Pennington, 1981; Taboada et al., 2000; Cortés et al., 2005). Other models consider the motion of the current plates, based on geodetic data, to support the orogen-parallel escape of the Northern Andes (e.g., Trenkamp et al., 2002; Mora-Páez et al., 2019). At deeper levels, slab flattening of the Nazca Plate and the hydration of the asthenospheric wedge are invoked to explain the topographic uplift of the

northern EC north of latitude 5°N (e.g., Chiarabba et al., 2016; Monsalve et al., 2019; Siravo et al., 2019b). Other authors propose slab break-off of the Caribbean Plate beneath the Santander Massif (Bucaramanga nest), ultimately inducing uplift, magmatism, and hydrothermal and seismic activity (Vargas and Mann, 2013; Bernet et al., 2016; Amaya et al., 2017; Vargas, 2020). More locally, tectonic inversion of master normal faults and thick-skin tectonics may have played a key role in topographic building (e.g., Dengo and Covey, 1993; Mora et al., 2010b). Although we cannot rule out any of the models mentioned above, we acknowledge that upper crustal shortening and thickening could explain the observed exhumation and topographic patterns for the EC. We further detail our reasoning below.

A closer look at the distribution of exhumation/erosion rates allows us to recognize two major events since the Neogene (Figs. 5 to 8): a regional event that built most of the EC and a younger Pliocene – Pleistocene event that was controlled by active faulting. Based on the swath analysis performed, the post-Miocene fault-controlled event induced rapid exhumation and high erosion rates (> 1 km/Myr) in faulted blocks delimited by inherited structures (e.g., Servitá and Pajarito Faults). The most significant differences are visible in SEC2, particularly between the Servitá and Bituima – Alto del Trigo Faults (Fig. 6). Considering that the climate proxy shows a poor spatial correlation with long-term erosion rates (erAFT, Fig. 10D), we propose below a mechanism based on previous studies and our interpretations of the compiled thermochronological data.

The along-strike exhumation and topographic changes in the eastern foothills are, in our interpretation, related to different fault geometries and deformation styles that guided deformation at shallower crustal levels (Mora et al., 2010b; Ramírez-Arias et al., 2012). We reason that where a steep major crustal fault ramp exists (such as the Servitá Fault), rapid exhumation, high long-term (erAFT) and short-term (erCN) erosion rates, and a stepped topography are observed (e.g., SEC2, Fig. 6). Furthermore, orographic rainfall is enhanced. Mora et al. (2006, 2009, 2010b) already envisaged, for instance, how the Servitá Fault underwent tectonic reactivation in thick-skinned tectonics, maintaining its high angle dip inherited from the Mesozoic extensional phase. This translates into long-term erosion rates higher than 2 km/Myr in the Quetame Massif (Fig. 6). In other words, Mesozoic rift tectonics controlled Cenozoic Andean syn-orogenic erosional exhumation of the EC as recently proposed by Pérez-Consuegra et al. (2021). These authors, who presented new low-temperature thermochronological data for the southern EC, concluded that the tectonic inheritance of the Cretaceous Basin controlled the location and amount of exhumation in the Andean orogeny instead of modern climate proxies.

In contrast, when the main fault shows a flatter detachment and thin-skinned tectonics, there is no further exhumation. For instance, the Guaicaramo thrust south of latitude 4°45'N is a low-angle (< 30°) decollement ramp in a thin-skinned style (Mora et al., 2006; 2010b; Fig 12). Further north, we computed moderate to low erAFT (below 1.0 km/Myr; Fig. 8) in an area where the Guaicaramo Fault transmits part of the strain to the more frontal Cusiana and Yopal Faults that eventually accommodate more than 1.5 km of vertical displacement (Mora et al., 2006; see also Cazier et al., 1995). For the western foothills, none of the inherited structures (e.g., La Salina-Bituima thrusts) experienced tectonic inversion as did the Servitá Fault, and thus, their structural style, along with other thrusts such as the Cambao and Honda Faults, is more similar to the Guaicaramo thrust (Mora et al., 2010a). These structures exhibit a ramp-flat-ramp geometry (Mon.es et al., 2003), with moderate erAFT around 1.0 km/Myr (Fig. 6).

In summary, we reason that fault geometry (ramp vs flat geometry, thick- vs thin-skin tectonics), together with the geometry of the inherited faults and the thickness and the geometry of the basin (width), regulate the structural and topographic evolution of the orogen, enhancing the occurrence of oblique faults (e.g., the Servitá Fault) (cf. Jara et al., 2015). Further, this structural setup also controls modern-day seismicity, extending foreward in the north (accommodated co-seismically by reverse/thrust faulting featuring low b-values; Fig. 9B) and continuing in the foothills in the south (in oblique contraction with a dextral slip component) (Fig. 2). This hypothesis agrees with a model proposed to explain the along-strike variations in kinematics, exhumation, and topography in the Himalayas, which proposes that when crustal ramps are present, high exhumation rates and stream incision can be predicted (Robert et al., 2011; van der Beek et al., 2016).

7.4 The uplift of the EC: the role of the Servitá and Algeciras Faults

The Servitá and Algeciras faults are, in our interpretation, two of the most conspicuous structures in the EC. The inversion of the Servitá Fault was promoted and controlled by fault orientation and the hanging wall stratigraphic sequence thickness (Mora et al., 2009; Tesón et al., 2013). Both faults are responsible for the rapid exhumation of the Quetame Massif in the Pliocene – Pleistocene (Anderson et al., 2015; Pérez-Consuegra et al., 2021). Associated with these structures, we obtained high erAFT (up to 3 km/Myr, the highest in the study area), high ksn values (>240), in addition to a rugged topography with V-shaped valleys, and high 5 km-radius relief (>2 km) supporting a tectonically active landscape. The highest median seismic strain rate (SSR16, Fig. 9D) and seismic

uplift rate (u16, Fig. 9F) among all subregions were obtained in SEC2E, associated with the Servitá Fault.

Previous estimates of surface uplift for the EC in the axial plateau based on paleobotanical evidence invoke a net uplift of at least 1.3 km, mostly occurring between 2 and 5 Ma (Wijninga, 1996; Gregory-Wodzicki, 2000). More recently, Anderson et al. (2015) provided new estimations of late Cenozoic surface uplift of the EC, suggesting no more than 1000 m of surface uplift from 7.6 Ma to the present. Considering these estimations belong to the EC axial plateau, and considering the observed diachronous exhumation pattern, these cannot be extrapolated to the entire range. Nevertheless, our estimations of surface uplift of the Sumapaz-Chingaza subdued landscapes agree with more than 1 km of net surface uplift since at least the Late Miocene, when the latest and faster exhumation event was recorded in the area (Mora et al., 2008; 2010b). This magnitude matches the seismic uplift (u16) distribution for subregion SEC2E in the past 5 Ma (Fig. 9). Additional constraints on the uplift of the Quetame Massif were provided by Mora et al. (2010b), who reported ~3 km of rock uplift for the Boa thrust's hanging wall (a shortcut of the Servitá Fault). For this reason, we consider that a surface uplift (rock uplift minus denudation) of 1.4 km could be possible.

In summary, we interpret the post-Miocene surface uplift of the Sumapaz and Chingaza páramos to have been controlled by the Servitá and Algeciras faults in a transpressional setting. The high present-day erCN provided by Struth et al. (2016), the high relief (Fig. 6), and ksn patterns support a Plio-Quaternary activity for these structures. Moreover, both structures present high seismic rates with moderate magnitude earthquakes recorded in the past 20 years, such as the recent Mesetas Earthquake (Mw = 6.0) on 24 December 2019 (Fig. 2) (Noriega-Londoño et al., 2021). A thickened crust resulting from Cenozoic shortening and a more recent isostatic response may have helped uplift the Chingaza and Sumapaz landscapes. Nonetheless, a deeper (mantle) source for the 1.4 km surface uplift cannot be ruled out. For instance, Garzione et al. (2008) proposed lower crustal removal as the trigger of rapid Late Miocene to Pliocene surface uplift of between 1.5 and 2.5 km for the Altiplano region in the Central Andes. If the uplift described here is feasible and well-constrained in time (based on the AFT data by Mora et al., 2008, 2010b), and considering the moderate to low Quaternary shortening rates for the eastern foothills (between 2.1±1.2 mm/yr (Veloza et al., 2015) and 4.1 mm/yr (Mora-Páez et al., 2019)), then the hypothesis postulated by Garzione et al. (2008) could also work for the central-southern part (south of latitude 4°N) of the EC. In the northern part of the EC, Siravo et al. (2019b) recently proposed a flat slab mechanism to explain the highest elevations achieved at the SNC (Fig. 1A). New paleoelevation constraints, preferably outside the Bogotá Basin, are required to understand the construction of the páramos

landscapes and the uplift of this area. These studies would not only contribute to the discussion on the morphology of the Andes but would also greatly impact the understanding of how the growth of the Andes influenced these paramo ecosystems (e.g., Hoorn et al., 2010; Antonelli et al., 2018; Flantua et al., 2019), thus leading to the explosion in biodiversity.

8. Conclusions

We compiled a significant dataset of apatite fission-track data (n = 312) from which we analyzed the long-term erosion rates (erAFT) for six subregions (SEC2W, SEC2E, SEC3C, SEC4W, SEC4C, and SEC4E) of the EC in the Colombian Northern Andes and their possible drivers (rainfall and/or tectonics). The following conclusions can be drawn from this analysis:

High erosion rates (> 2 km/Myr) were calculated only in the Quetame Massif, at subzone SEC2E, whereas the rest of the EC is characterized by moderate to low erAFT (< 1 km/Myr). This high erAFT also coincides with high published catchment-wide erosion rates (> 400 mm/ka) derived from ^{10}Be terrestrial cosmogenic nuclides. However, we computed a tenfold difference between erAFT and erCN despite high rainfall rates (~3700 mm/yr). We hypothesize that massive channel aggradation in a seismically active region is responsible for modifying river dynamics and delaying the erosional response of the drainage system to the imposed high rock uplift rates.

We have not found statistical support for a climate-driven exhumation event in the EC, except for a partial spatial correlation in subzone SEC2E, where this hypothesis was proposed by Mora et al. (2008). The western foothills in swaths SEC3 and SEC4 showed similar rainfall rates as subzone SEC2E, however erosion rates were two to three times higher in the latter. In this area, we observed a tenfold difference between erAFT and erCN, suggesting a decoupling in erosion rates despite the high rainfall rates. These observations also cast doubt on of the influence of climate on the topographic asymmetry of the EC.

For subzone SEC2E, where the highest erosion rates were computed, we interpreted the Servitá Fault as the main structure responsible for the topographic construction of the Quetame massif. We propose tectonic inheritance in a transpressional stress state as the mechanism responsible for the diachronous exhumation of the EC and the subsequent uplift of the range.

The seismic parameters (seismic strain rate or seismic energy) explain long-term erosion rates in most subregions, suggesting that coseismic deformation predicts erosion rates, while climate plays a second or more local role in controlling erosion. In subzones SEC4C and SEC4E, we obtained a

decoupling between erAFT and seismic parameters that potentially reflects aseismic deformation or low tectonic activity. For these areas, the ksn stand out as a significant predictor of erAFT, which supports the aseismic deformation hypothesis.

Based on projected paleoprofiles of four rivers (the Duda, Ariari, Guayuriba and Guatiquiá Rivers) draining the Sumapaz and Chingaza low-relief landscapes, we estimated a post-Miocene surface uplift of at least 1.4 km concentrated on the hanging wall of the Algeciras-Servitá fault system. These findings reinforce the influence of tectonic inheritance in controlling the long-term structural development of an inverted orogen, including the exhumation rates and the short-term landscape evolution.

Acknowledgments

H.G.D. is grateful to Nicolás Pérez for the invitation to take part in a six-day field trip along the Duda River that served as inspiration for this manuscript. M.A.B acknowledges the financial support provided by the Universidad Pedagógica y Tecnológica de Colombia (UPTC), DIN SGI Project 3104. The authors thank Luis Palazzesi for his guest editorial handling and two anonymous reviewers who provided valuable comments that greatly improved this manuscript. Also, we want to thank Amelia Bain for her support in reviewing the style and grammar of this article.

Conflicts of Interest Statement

The authors certify that they have NO affiliations with or involvement in any organization or entity with any financial interest (such as honoraria; educational grants; participation in speakers' bureaus; membership, employment, consultancies, stock ownership, or other equity interest; and expert testimony or patent-licensing arrangements), or non-financial interest (such as personal or professional relationships, affiliations, knowledge or beliefs) in the subject matter or materials discussed in this manuscript.

Supplementary data

Supplementary table 1

Supplementary table 2

Supplementary table 3

Supplementary material 1

References

Abrahami, R., van der Beek, P., Huyghe, P., Hardwick, E., Carcaillet, J., 2016. Decoupling of long-term exhumation and short-term erosion rates in the Sikkim Himalaya. Earth Planet. Sci. Lett. 433, 76–88. https://doi.org/10.1016/j.epsl.2015.10.039

Acosta, J., Velandia, F., Osorio, J., Lonergan, L., Mora, H., 2007. Strike-slip deformation within the Colombian Andes.Deformation of the continental crust. Geological Society of London, Special Publications 272, 303–319.

Akaike, H., 1974. A New look at the statistical model identification. IEEE Trans. Automat. Contr. 19, 716–723. https://doi.org/10.1109/TAC.1974.1100705

Albert, J.S., Val, P., Hoorn, C., 2018. The changing course of the Amazon River in the Neogene: center stage for Neotropical diversification. Neotropical Ichthyology 16, 1-24. https://doi.org/10.1590/1982-0224-20180033

Alfaro–Valero, C.M., Rueda–Gutierrez, J.B., Matiz–León, J.C., Beltrán–Luque, M.A., Rodríguez–Rodríguez, G.F., Rodríguez–Ospina, G.Z., González–Idárraga, C.E., and Malo–Lázaro, J.E., 2020. Paipa Geothermal System, Boyacá: Review of Exploration Studies and Conceptual Model, in Gómez, J. and Pinilla–Pachón, A.O. eds., The Geology of Colombia, Bogotá, Colombia, Servicio Geológico Colombiano, Publicaciones Geológicas Especiales 36, v. 4, pp 36. https://doi.org/10.32685/pub.esp.38.2019.04

Amaya, S., Zuluaga, C.A., Bernet, M., 2017. New fission-track age constraints on the exhumation of the central Santander Massif: Implications for the tectonic evolution of the Northern Andes, Colombia. Lithos 282–283, 388–402. https://doi.org/10.1016/j.lithos.2017.03.019

Amaya, S., Zuluaga, C.A., Bernet, M., 2020. Different Levels of Exhumation across the Bucaramanga Fault in the Cepitá Area of the Southwestern Santander Massif, Colombia: Implications for the Tectonic Evolution of the Northern Andes in Northwestern South America, in Gómez, J. and Mateus-Zabala, D. eds., The Geology of Colombia, Bogotá, Colombia, Servicio Geológico Colombiano, Publicaciones Geológicas Especiales 37, v. 3, pp 17. https://doi.org/10.32685/pub.esp.37.2019.17

Anderson, V.J., Saylor, J.E., Shanahan, T.M., Horton, B.K., 2015. Paleoelevation records from lipid biomarkers: Application to the tropical Andes. Bull. Geol. Soc. Am. 127, 1604–1616. https://doi.org/10.1130/B31105.1

Andreani, L., Gloaguen, R., 2016. Geomorphic analysis of transient landscapes in the Sierra Madre de Chiapas and Maya Mountains (northern Central America): Implications for the North American-Caribbean-Cocos plate boundary. Earth Surf. Dyn. 4, 71–102. https://doi.org/10.5194/esurf-4-71-2016

Andriessen, P.A.M., Helmens, K.F., Hooghiemstra, H., Riezebos, P.A., van der Hammen, T., 1993. Absolute

chronology of the Pliocene-Quaternary sediment sequence of the Bogota area, Colombia. Quat. Sci. Rev. 12, 483–501. https://doi.org/10.1016/0277-3791(93)90066-U

Antonelli, A., Kissling, W.D., Flantua, S.G.A., Bermúdez, M.A., Mulch, A., Muellner-Riehl, A.N., Kreft, H., Linder, H.P., Badgley, C., Fjeldså, J., Fritz, S.A., Rahbek, C., Herman, F., Hooghiemstra, H., Hoorn, C., 2018. Geological and climatic influences on mountain biodiversity. Nat. Geosci. 11, 718–725. https://doi.org/10.1038/s41561-018-0236-z

Audemard, F.A., 1999. Morpho-structural expression of active thrust fault systems in the humid tropical foothills of Colombia and Venezuela. Zeitschrift für Geomorphol. 118, 227–244

Azañón, J.M., Galve, J.P., Pérez-Peña, J. V., Giaconia, F., Carvajal, R., Booth-Rea, G., Jabaloy, A., Vázquez, M., Azor, A., Roldán, F.J., 2015. Relief and drainage evolution during the exhumation of the Sierra Nevada (SE Spain): Is denudation keeping pace with uplift? Tectonophysics 663, 19–32. https://doi.org/10.1016/j.tecto.2015.06.015

Baldwin, J.A., Whipple, K.X., Tucker, G.E., 2003. Implications of the shear stress river incision model for the timescale of postorogenic decay of topography. J. Geophys. Res. Solid Earth 108. https://doi.org/10.1029/2001jb000550

Bande, A., Horton, B., Ramírez, J.C., Mora, A., Parra, M., Stockli, D., 2012. Clastic deposition, provenance, and sequence of Andean thrusting in the frontal Eastern Cordillera and Llanos foreland basin of Colombia. Bull. Geol. Soc. Am. 124, 53–76. https://doi.org/10.1130/B30412.1

Bassin, C., Laske, G., Masters, G., 2000. The Current Limits of Resolution for Surface Wave Tomography in North America, EOS Trans AGU 81, F897

Bayona, G., Cortés, M., Jaramillo, C., Ojeda, G., Aristizabal, J.J., Reyes-Harker, A., 2008. An integrated analysis of an orogen-sedimentary basin pair: Latest Cretaceous-Cenozoic evolution of the linked Eastern Cordillera orogen and the Llanos foreland basin of Colombia. Bull. Geol. Soc. Am. 120, 1171–1197. https://doi.org/10.1130/B26187.1

Bayona, G., Cardona, A., Jaramillo, C., Mora, A., Montes, C., Caballero, V., Mahecha, H., Lamus, F., Montenegro, O., Jimenez, G., Mesa, A., Valencia, V., 2013. Onset of fault reactivation in the Eastern Cordillera of Colombia and proximal Llanos Basin; response to Caribbean–South American convergence in early Palaeogene time. Geol. Soc. London, Spec. Publ. 377, 285–314. https://doi.org/10.1144/SP377.5

Bernet, M., 2019, Exhumation Studies of Mountain Belts Based on Detrital Fission-Track Analysis on Sand and Sandstones, *in* Fission-Track Thermochronology and its Application to Geology, Springer Textbooks in Earth Sciences, Geography and Environment, p. 269–277, doi:10.1007/978-3-319-89421-8_15.

Parra, M., Mora, A., Jaramillo, C., Strecker, M.R., Sobel, E.R., Quiroz, L., Rueda, M., and Torres, V., 2009a, Orogenic wedge advance in the northern Andes: Evidence from the Oligocene-Miocene sedimentary record of the Medina Basin, Eastern Cordillera, Colombia: Bulletin of the Geological Society of America, v. 121, p. 780–800, doi:10.1130/B26257.1.

Parra, M., Mora, A., Sobel, E.R., Strecker, M.R., and González, R., 2009b, Episodic orogenic front migration in the northern Andes: Constraints from low-temperature thermochronology in the Eastern Cordillera, Colombia: Tectonics, v. 28, doi:10.1029/2008TC002423.

Pérez-Consuegra, N., Hoke, G.D., Mora, A., Fitzgerald, P., Sobel, E.R., Sandoval, J.R., Glodny, J., Valencia, V., Parra, M., and Zapata, S., 2021, The Case for Tectonic Control on Erosional Exhumation on the Tropical Northern Andes Based on Thermochronology Data: Tectonics, v. 40, doi:10.1029/2020tc006652.

Ramirez-Arias, J.C., Mora, A., Rubiano, J., Duddy, I., Parra, M., Moreno, M., Stockli, D., and Casallas, W., 2012, The asymmetric evolution of the Colombian Eastern Cordillera. Tectonic inheritance or climatic forcing? New evidence from thermochronology and sedimentology: Journal of South American Earth Sciences, v. 39, p. 112–137, doi:10.1016/j.jsames.2012.04.008.

Reiners, P.W., and Brandon, M.T., 2006, Using Thermochronology To Understand Orogenic Erosion: Annual Review of Earth and Planetary Sciences, v. 34, p. 419–466, doi:10.1146/annurev.earth.34.031405.125202.

Bermúdez, M.A., Kohn, B.P., Van Der Beek, P.A., Bernet, M., O'Sullivan, P.B., Shagam, R., 2010. Spatial and temporal patterns of exhumation across the Venezuelan Andes: Implications for Cenozoic Caribbean geodynamics. Tectonics 29. https://doi.org/10.1029/2009TC002635

Bermúdez, M.A., van der Beek, P., Bernet, M., 2011. Asynchronous miocene-pliocene exhumation of the central venezuelan andes. Geology 39, 139–142. https://doi.org/10.1130/G31582.1

Bermúdez, M.A., Van der Beek, P.A., Bernet, M., 2013. Strong tectonic and weak climatic control on exhumation rates in the Venezuelan Andes. Lithosphere 5, 3–16. https://doi.org/10.1130/L212.1

Bermúdez, M.A., Hoorn, C., Bernet, M., Carrillo, E., van der Beek, P.A., Garver, J.I., Mora, J.L., Mehrkian, K., 2017. The detrital record of late-Miocene to Pliocene surface uplift and exhumation of the Venezuelan Andes in the Maracaibo and Barinas foreland basins. Basin Res. 29, 1–26. https://doi.org/10.1111/bre.12154

Bermúdez, M.A., Bernet, M., Kohn, B.P., Brichau, S., 2019. Exhumation-Denudation History of the Maracaibo Block, Northwestern South America: Insights from Thermochronology. In: Cediel, F., Shaw, R.P. (Eds.) Geology and Tectonics of Northwestern South America. Frontiers in Earth Sciences, pp. 879 – 898.

Bermúdez, M.A., Velandia, F., García-Delgado, H., Jiménez, D., Bernet, M., 2021. Exhumation of the southern transpressive Bucaramanga fault, eastern Cordillera of Colombia: Insights from detrital, quantitative thermochronology and geomorphology. J. South Am. Earth Sci. 106, 103057. https://doi.org/10.1016/j.jsames.2020.103057

Bernet, M., 2019. Exhumation Studies of Mountain Belts Based on Detrital Fission-Track Analysis on Sand and Sandstones, in Fission-Track Thermochronology and its Application to Geology. Springer Textbooks in Earth Sciences, Geography and Environment. 269–277, https://doi.org/10.1007/978-3-319-89421-8_15.

Bonnet, S., Crave, A., 2003. Landscape response to climate change: Insights from experimental modeling and implications for tectonic versus climatic uplift of topography. Geology 31, 123–126. https://doi.org/10.1130/0091-7613(2003)031<0123:LRTCCI>2.0.CO;2

Bookhagen, B., 2013. High Resolution Spatiotemporal Distribution of Rainfall Seasonality and Extreme Events Based on a 12-year TRMM Time Series. UC Santa Barbara Geography

Bookhagen, B., Strecker, M.R., 2008. Orographic barriers, high-resolution TRMM rainfall, and relief variations along the eastern Andes. Geophys. Res. Lett. 35, 1–6. https://doi.org/10.1029/2007GL032011

Brandon, M.T., Roden-Tice, M.K., and Garver, J.I., 1998. Late Cenozoic exhumation of the Cascadia accretionary wedge in the Olympic Mountains, northwest Washington State. Geol. Soc. of Ame. Bull. 110, 985–1009. https://doi.org/10.1130/0016-7606(1998) 110<0985:LCEOTC>2.3.CO;2

Branquet, Y., Cheilletz, A., Cobbold, P.R., Baby, P., Laumonier, B., Giuliani, G., 2002. Andean deformation and rift inversion, eastern edge of Cordillera Oriental (Guateque-Medina area), Colombia. J. South Am. Earth Sci. 15, 391–407. https://doi.org/10.1016/S0895-9811(02)00063-9

Braun, J., Burbidge, D.R., Gesto, F.N., Sandiford, M., Gleadow, A.J.W., Kohn, B.P., Cummins, P.R., 2009. Constraints on the current rate of deformation and surface uplift of the Australian continent from a new seismic database and low-T thermochronological data. Australian J. of Earth Sci. 56, 99–110. https://doi.org/10.1080/08120090802546977

Braun, J., Simon-Labric, T., Murray, K.E., Reiners, P.W., 2014. Topographic relief driven by variations in surface rock density. Nat. Geosci. 7, 534–540. https://doi.org/10.1038/ngeo2171

Burbank, D.W., Blythe, A.E., Putkonen, J., Pratt-Sitaula, B., Gabet, E., Oskin, M., Barros, A., Ojha, T.P., 2003. Decoupling of erosion and rainfall in the Himalayas. Nature 426, 652–655. https://doi.org/10.1038/nature02187

Bustos, X., Bermúdez, M.A., Marín-Cerón, M.I., 2013. Comparación de superficies de erosión en el altiplano Antioqueño mediante geomorfología cuantitativa. Terra Nueva Etapa 46, 43-67

Caballero, V., Mora, A., Quintero, I., Blanco, V., Parra, M., Rojas, L.E., Lopez, C., Sánchez, N., Horton, B.K., Stockli, D., Duddy, I., 2013a. Tectonic controls on sedimentation in an intermontane hinterland basin adjacent to inversion structures: the Nuevo Mundo syncline, Middle Magdalena Valley, Colombia. Geol. Soc. London, Spec. Publ. 377, 315–342. https://doi.org/10.1144/SP377.12

Caballero, V., Parra, M., Mora, A., López, C., Rojas, L.E., Quintero, I., 2013b. Factors controlling selective abandonment and reactivation in thick-skin orogens: a case study in the Magdalena Valley, Colombia. Geol. Soc. London, Spec. Publ. 377, 343–367. https://doi.org/10.1144/SP377.4

Cederbom, C.E., Sinclair, H.D., Schlunegger, F., Rahn, M.K., 2004. Climate-induced rebound and exhumation of the European Alps. Geology 32, 709–712. https://doi.org/10.1130/G20491.1

Cediel, F., Shaw, R., Cáceres, C., 2003. Tectonic assembly of the northern Andean block. In: Bartolini, C., Buffler, R.T., Blickwede, J. (Eds.), The Circum-Gulf of Mexico and the Caribbean: Hydrocarbon Habitats, Basin Formation and Plate Tectonics, vol. 79. American Association of Petroleum Geologists Memoir, pp. 815–848.

Champagnac, J.D., Molnar, P., Anderson, R.S., Sue, C., Delacou, B., 2007. Quaternary erosion-induced isostatic rebound in the western Alps. Geology 35, 195–198. https://doi.org/10.1130/G23053A.1

Cheng, Q.M., Sun, H.Y., 2018. Variation of singularity of earthquake-size distribution with respect to tectonic regime. Geosci. Front. 9, 453–458. https://doi.org/10.1016/j.gsf.2017.04.006

Chiarabba, C., De Gori, P., Faccenna, C., Speranza, F., Seccia, D., Dionicio, V., Prieto, G.A., 2016. Subduction system and flat slab beneath the Eastern Cordillera of Colombia. Geochemistry, Geophys. Geosystems 17, 16–27. https://doi.org/10.1002/2015GC006048

Clark, M.K., Maheo, G., Saleeby, J., Farley, K.A., 2005. The non-equilibrium landscape of the southern Sierra Nevada, California. GSA Today 15, 4–10. https://doi.org/10.1130/1052-5173(2005)015[4:TNLOTS]2.0.CO;2

Clark, M.K., Royden, L.H., Whipple, K.X., Burchfiel, B.C., Zhang, X., Tang, W., 2006. Use of a regional, relict landscape to measure vertical deformation of the eastern Tibetan Plateau. J. Geophys. Res. Earth Surf. 111, 1–23. https://doi.org/10.1029/2005JF000294

Colombian Geological Survey, 2018. Actualización del Estudio de Zonificación de Amenaza por Movimientos en Masa a Escala 1:25.000 y la Zonificación de Amenaza por Movimientos en Masa Tipo Avenida Torrencial Escala 1:25.000 en el Municipio Villavicencio. Departamento del Meta. Convenio SGC-IGAC 02/2018. Internal report, pp. 414.

Cooper, M.A., Addison, F.T., Álvarez, R., Coral, M., Graham , R.H., Hayward, A.B., Howe, S., Martínez, J., Naar, J., Peñas , R., Pulham, A. J., and Taborda, A., 1995. Basin development and tectonic history of the Llanos Basin, Eastern Cordillera, and Middle Magdalena Valley, Colombia. Am. Assoc. Pet. Geol.

Bull. 79 (10), 1421–1423

Corredor, F., 2003. Eastward extent of the late Eocene-Early Oligocene onset of deformation across the northern Andes: Constraints from the northern portion of the Eastern Cordillera fold belt, Colombia. J. South Am. Earth Sci. 16, 445–457. https://doi.org/10.1016/j.jsames.2003.06.002

Cortés, M., Angelier, J., 2005. Current states of stress in the northern Andes as indicated by focal mechanisms of earthquakes. Tectonophysics 403, 29–58. https://doi.org/10.1016/j.tecto.2005.03.020

Delgado, A., Mora, A., Reyes-Harker, A., 2012. Deformation partitioning in the Llanos foreland basin during the Cenozoic and its correlation with mountain building in the hinterland. J. South Am. Earth Sci. 39, 228–244. https://doi.org/10.1016/j.jsames.2012.04.011

Dengo, C.A., Covey, M.C., 1993. Structure of the Eastern Cordillera of Colombia: implications for trap styles and regional tectonics. Am. Assoc. Pet. Geol. Bull. 77, 1315–1337. https://doi.org/10.1306/BDFF8E7A-1718-11D7-8645000102C1865D

DiBiase, R.A., Whipple, K.X., Heimsath, A.M., Ouimet, W.B., 2010. Landscape form and millennial erosion rates in the San Gabriel Mountains, CA. Earth Planet. Sci. Lett. 289, 134–144. https://doi.org/10.1016/j.epsl.2009.10.036

Dimate, C., Rivera, L., Taboada, A., Delouis, B., Osorio, A., Jimenez, E., Fuenzalida, A., Cisternas, A., Gomez, I., 2003. The 19 January 1995 Tauramena (Colombia) earthquake: Geometry and stress regime. Tectonophysics 363, 159–180. https://doi.org/10.1016/S0040-1951(02)00670-4

Egbue, O., Kellogg, J., 2010. Pleistocene to Present North Andean "escape." Tectonophysics 489, 248–257. https://doi.org/10.1016/j.tecto.2010.04.021

Ehlers, T. a., Chaudhri, T., Kumar, S., Fuller, C. w, Willett, S. d, Ketcham, R.A., Brandon, M.T., Belton, D.X., Kohn, B.P., Gleadow, A.J.W., Dunai, T.J., Fu, F.Q., 2005. Computational Tools for Low-Temperature Thermochronometer Interpretation. Rev. Mineral. Geochemistry 58, 589–622. https://doi.org/10.2138/rmg.2005.58.22

England, P., Molnar, P., 1990. Late Cenozoic uplift of mountain ranges and global climate change : chicken or egg? Nature 346, 29–34

Fabre, A., 1983. La subsidencia de la Cuenca del Cocuy (Cordillera Oriental de Colombia) durante el Cretáceo y el Terciario Inferior. Primera parte: Estudio cuantitativo de la subsidencia. Geol. Norandina 8, 22–27

Farris, D.W., Jaramillo, C., Bayona, G., Restrepo-Moreno, S.A., Montes, C., Cardona, A., Mora, A., Speakman, R.J., Glascock, M.D., Valencia, V., 2011. Fracturing of the Panamanian Isthmus during initial collision with: South America. Geology 39, 1007–1010. https://doi.org/10.1130/G32237.1

Flantua, S.G.A., O'Dea, A., Onstein, R.E., Giraldo, C., Hooghiemstra, H., 2019. The flickering connectivity system of the north Andean páramos. J. Biogeogr. 46, 1808–1825. https://doi.org/10.1111/jbi.13607

Flint, J.J., 1974. Stream Gradient as a Function of Order, Magnitude, and Discharge. Water Resour. Res. 10, 969–973

Forte, A.M., Whipple, K.X., 2018. Short communication: The Topographic Analysis Kit (TAK) for TopoToolbox. Earth Surf. Dyn. Discuss. 1–9. https://doi.org/10.5194/esurf-2018-57

Frohlich, C., Davis, S., 1993. Teleseismic b Values; Or, Much Ado About 1.0. J. Geophys. Res. 98, 631–644

Galbraith, R.F., 1981. On statistical models for fission track counts. J. Int. Assoc. Math. Geol. 13, 471–478. https://doi.org/10.1007/BF01034498

García, H., Jiménez, G., 2016. Transverse zones controlling the structural evolution of the Zipaquira Anticline (Eastern Cordillera, Colombia): Regional implications. J. South Am. Earth Sci. 69, 243–258. https://doi.org/10.1016/j.jsames.2016.04.002

Gasparini, N.M., Whipple, K.X., 2014. Diagnosing climatic and tectonic controls on topography: Eastern flank of the northern Bolivian Andes. Lithosphere 6, 230–250. https://doi.org/10.1130/L322.1

Godano, C., Lippiello, E., De Arcangelis, L., 2014. Variability of the b value in the Gutenberg-Richter distribution. Geophys. J. Int. 199, 1765–1771. https://doi.org/10.1093/gji/ggu359

Godard, V., Bourlès, D.L., Spinabella, F., Burbank, D.W., Bookhagen, B., Fisher, G.B., Moulin, A., Léanni, L., 2014. Dominance of tectonics over climate in Himalayan denudation. Geology 42, 243–246. https://doi.org/10.1130/G35342.1

Gómez, H. 1991. La Paleomegacizalla Transversal de Colombia, Base para un Nuevo Esquema Geotectónico. Revista CIAF., Bogotá, Vol. 12 (1), 49-61.

Gómez, E., 2001. Tectonic controls on the late Cretaceous to Cenozoic sedimentary fill of the Middle Magdalena Valley Basin, Eastern Cordillera and Llanos Basin, Colombia. ProQuest Diss. Theses

Gómez, E., Jordan, T.E., Allmendinger, R.W., Hegarty, K., Kelley, S., Heizler, M., 2003. Controls on architecture of the Late Cretaceous to Cenozoic southern. GSA Bull. 115, 131–147. https://doi.org/10.1130/0016-7606(2003)115<0131

Gómez, J., Montes, N.E., Nivia, Á., Diederix, H., compilers. 2015. Geological Map of Colombia 2015. Scale 1:1000000. Servicio Geológico Colombiano, 2 sheets. Bogotá.

Green, P.F., 1981. A new look at statistics in fission-track dating. Nucl. Tracks 5, 77–86. https://doi.org/10.1016/0191-278X(81)90029-9

Gregory-Wodzicki, K.M., 2000. Uplift history of the Central and Northern Andes: A review. Geol. Soc. Am.

Bull. 112, 1091–1105. https://doi.org/10.1130/0016-7606(2000)112<1091:UHOTCA>2.0.CO;2

Guerrero, J., 2018. Pre-Andean tectonic events from Albian to Eocene in the Middle Magdalena and the situation of the western flank of the Prot-Eastern Cordillera. Dissertation PhD Thesis

Gutenberg, B., Richter, C.F., 1944. Frequency of earthquakes in California. Bull. Seismol. Soc. Am. 34, 185–188. https://doi.org/10.1038/156371a0

Gutscher, M.A., Malavieille, J., Lallemand, S., Collot, J.Y., 1999. Tectonic segmentation of the North Andean margin: Impact of the Carnegie Ridge collision. Earth Planet. Sci. Lett. 168, 255–270. https://doi.org/10.1016/S0012-821X(99)00060-6

Helmens, K.F., 1988. Late Pleistocene glacial sequence in the area of the high plain of Bogotá (Eastern Cordillera, Colombia). Palaeogeogr. Palaeoclimatol. Palaeoecol. 67. https://doi.org/10.1016/0031-0182(88)90156-3

Helmens, K.F., Rutter, N.W., Kuhry, P., 1997. Glacier fluctuations in the Eastern Andes of Colombia (south America) during the last 45,000 radiocarbon years. Quat. Int. 38–39, 39–48. https://doi.org/10.1016/S1040-6182(96)00021-3

Herman, F., Seward, D., Valla, P.G., Carter, A., Kohn, B., Willett, S.D., Ehlers, T.A., 2013. Worldwide acceleration of mountain erosion under a cooling climate. Nature 504, 423–426. https://doi.org/10.1038/nature12877

Hernández-Chaparro, D., Bermúdez, M.A., Rubio, G., García-Delgado, H., Machuca, S., 2021. Discriminación de la relación precipitación-tectónica como agentes modeladores del paisaje en los alrededores del Municipio Guayabetal, Cordillera Oriental de Colombia. Boletín de la Sociedad Geológica Mexicana. http://dx.doi.org/10.18268/BSGM2021v73n2a120121

Hoke, G.D., Isacks, B.L., Jordan, T.E., Blanco, N., Tomlinson, A.J., Ramezani, J., 2007. Geomorphic evidence for post-10 Ma uplift of the western flank of the central Andes 18°30′ - 22°S. Tectonics 26, 1–17. https://doi.org/10.1029/2006TC002082

Holt, W.E., Shen-Tu, B., Haines, J., Jackson J., 2000. On the determination of self-consistent strain rate fields within zones of distributed continental deformation, in Richards, M.A., Gordon, R.G., and van der Hilst, R.D., (Eds.), The History and Dynamics of Global Plate Motions: American Geophysical Union, Washington, D.C., Geophysical Monograph Series 121, pp. 113–141

Hooghiemstra, H., 1989. Quaternary and upper-pliocene glaciations and forest development in the tropical andes: Evidence from a long high-resolution pollen record from the sedimentary basin of Bogotá, Colombia. Palaeogeogr. Palaeoclimatol. Palaeoecol. 72, 11–26. https://doi.org/10.1016/0031-0182(89)90129-6

Hooghiemstra, H., van der Hammen, T., 1993. Late quaternary vegetation history and paleoecology of Laguna Pedro Palo (subandean forest belt, Eastern Cordillera, Colombia). Rev. Palaeobot. Palynol. 77, 235–262. https://doi.org/10.1016/0034-6667(93)90006-G

Hoorn, C., 1994. An environmental reconstruction of the palaeo-Amazon River system (Middle-Late Miocene, NW Amazonia). Palaeogeogr. Palaeoclimatol. Palaeoecol. 112, 187–238. https://doi.org/10.1016/0031-0182(94)90074-4

Hoorn, C., Guerrero, J., Sarmiento, G.A., Lorente, M.A., 1995. Andean tectonics as a cause for changing drainage patterns in Miocene northern South America. Geology 23, 237–240. https://doi.org/10.1130/0091-7613(1995)023<0237

Hoorn, C., Wesselingh, F.P., ter Steege, H., Bermudez, M.A., Mora, A., Sevink, J., Sanmartín, I., Sanchez-Meseguer, A., Anderson, C.L., Figueiredo, J.P., Jaramillo, C., Riff, D., Negri, F.R., Hooghiemstra, H., Lundberg, J., Stadler, T., Särkinen, T., Antonelli, A., 2010. Amazonia Through Time : Andean Uplift, Climate Change, Landscape Evolution and Biodiversity. Science (80-.). 330, 927–931. https://doi.org/10.1126/science.1194585

Jara, P., Likerman, J., Winocur, D., Ghiglione, M.C., Cristallini, E.O., Pinto, L., Charrier, R., 2014. Role of basin width variation in tectonic inversion: insight from analogue modelling and implications for the tectonic inversion of the Abanico Basin, 33°–34°S, Central Andes, in: Sepúlveda, S.A., Giambiagi, L.B., Moreiras, S.M., Pinto, L., Tunik, M., Hoke, G.D., Farías, M. (Eds.), Geodynamic Processes in the Andes of Central Chile and Argentina. Geological Society, Special Publication 399, London, pp. 83-107

Jiménez, G., Speranza, F., Faccenna, C., Bayona, G., Mora, A., 2014. Paleomagnetism and magnetic fabric of the Eastern Cordillera of Colombia: Evidence for oblique convergence and non rotational reactivation of a Mesozoic intracontinental rift. Tectonics 33, 2233–2260. https://doi.org/10.1002/2014TC003532

Kaandorp, R.J.G., Vonhof, H.B., Wesselingh, F.P., Pittman, L.R., Kroon, D., Van Hinte, J.E., 2005. Seasonal Amazonian rainfall variation in the Miocene climate optimum. Palaeogeogr. Palaeoclimatol. Palaeoecol. 221, 1–6. https://doi.org/10.1016/j.palaeo.2004.12.024

Kammer, A., 1996. Estructuras y Deformaciones del Borde Oriental del Macizo de Floresta. Geol. Colomb. 21, 65–80

Kammer, A., 1999. Observaciones acerca de un origen transpresivo de la Cordillera Oriental. Geol. Colomb. 24, 29–53.

Keller, E., Pinter, N., 2002. Active Tectonics: Earthquakes, uplift and landscape, second. ed, Pearson Education. Pearson Education

Ketcham, R. a, Donelick, R. a, Carlson, W.D., 1999. Variability of apatite fission-track annealing kinetics. III. Extrapolation to geological time scales. Am. Mineral. 84, 1235–1255.

https://doi.org/10.2138/am.2006.464

Kirby, E., Whipple, K., 2001. Quantifying differential rock-uplift rates via stream profile analysis. Geology 29, 415. https://doi.org/10.1130/0091-7613(2001)029<0415:QDRURV>2.0.CO;2

Kirby, E., Whipple, K.X., Tang, W., Chen, Z., 2003. Distribution of active rock uplift along the eastern margin of the Tibetan Plateau: Inferences from bedrock channel longitudinal profiles. J. Geophys. Res. Solid Earth 108. https://doi.org/10.1029/2001JB000861

Kirby, E., Whipple, K., Harkins, N., 2008. Topography reveals seismic hazard. Nat. Geosci. 1, 485–487. https://doi.org/10.1038/ngeo265

Kirby, E., Whipple, K.X., 2012. Expression of active tectonics in erosional landscapes. J. Struct. Geol. 44, 54–75. https://doi.org/10.1016/j.jsg.2012.07.009

Korup, O., 2006. Rock-slope failure and the river long profile. Geology 34, 45–48. https://doi.org/10.1130/G21959.1

Kuhry, P., Hooghiemstra, H., van Geel, B., van der Hammen, T., 1993. The El Abra stadial in the Eastern Cordillera of Colombia (South America). Quat. Sci. Rev. 12, 333–343. https://doi.org/10.1016/0277-3791(93)90041-J

Laske, G., Masters., G., Ma, Z., Pasyanos, M., 2013. Update on CRUST1.0 - A 1-degree Global Model of Earth's Crust, Geophys. Res. Abstracts, 15, Abstract EGU2013-2658

Menéndez, I., Silva, P.G., Martín-Betancor, M., Pérez-Torrado, F.J., Guillou, H., Scaillet, S., 2008. Fluvial dissection, isostatic uplift, and geomorphological evolution of volcanic islands (Gran Canaria, Canary Islands, Spain). Geomorphology 102, 189–203. https://doi.org/10.1016/j.geomorph.2007.06.022

Molin, P., Pazzaglia, F., Dramis, F., 2004. Geomorphic expression of active tectonics in a rapidly-deforming forearc, Sila Massif, Calabria, southern Italy. Am. J. Sci. 304, 559–589. https://doi.org/10.2475/ajs.304.7.559

Molnar, P., 2004. Late Cenozoic increase in accumulation rates of terrestrial sediment: How might climate change have affected erosion rates? Annu. Rev. Earth Planet. Sci. 32, 67–89. https://doi.org/10.1146/annurev.earth.32.091003.143456

Monsalve, G., Jaramillo, J.S., Cardona, A., Schulte-Pelkum, V., Posada, G., Valencia, V., Poveda, E., 2019. Deep Crustal Faults, Shear Zones, and Magmatism in the Eastern Cordillera of Colombia: Growth of a Plateau From Teleseismic Receiver Function and Geochemical Mio-Pliocene Volcanism Constraints. J. Geophys. Res. Solid Earth 124, 9833–9851. https://doi.org/10.1029/2019JB017835

Montes, C., Restrepo-Pace, P., Hatcher Jr, R., 2003. Three-dimensional Structure and Kinematics of the Piedras-Girardot Fold Belt: Surface Expression of Transpressional Deformation in the Northern Andes,

in: Bartolini, C., Buffler, R.T., Blickwede, J. (Eds.), The Circum-Gulf of Mexico and the Caribbean: Hydrocarbon Habitats, Basin Formation, and Plate Tectonics. pp. 849–873

Montgomery, D.R., Balco, G., Willett, S.D., 2001. Climate, Tectonics, and the Morphology of the Andes. Geology 29, 579–582. https://doi.org/10.1130/0091-7613(2001)029<0579

Montgomery, D.R., Brandon, M.T., 2002. Topographic controls on erosion rates in tectonically active mountain ranges. Earth Planet. Sci. Lett. 201, 481–489. https://doi.org/10.1016/S0012-821X(02)00725-2

Mora-Páez, H., Kellogg, J.N., Freymueller, J.T., Mencin, D., Fernandes, R.M.S., Diederix, H., LaFemina, P., Cardona-Piedrahita, L., Lizarazo, S., Peláez-Gaviria, J.-R., Díaz-Mila, F., Bohórquez-Orozco, O., Giraldo-Londoño, L., Corchuelo-Cuervo, Y., 2019. Crustal deformation in the northern Andes – A new GPS velocity field. J. South Am. Earth Sci. https://doi.org/10.1016/j.jsames.2018.11.002

Mora, A., Parra, M., Strecker, M.R., Kammer, A., Dimaté, C., Rodríguez, F., 2006. Cenozoic contractional reactivation of Mesozoic extensional structures in the Eastern Cordillera of Colombia. Tectonics 25, 1–19. https://doi.org/10.1029/2005TC001854

Mora, A., Parra, M., Strecker, M.R., Sobel, E.R., Hooghiemstra, H., Torres, V., Jaramillo, J.V., 2008. Climatic forcing of asymmetric orogenic evolution in the Eastern Cordillera of Colombia. Bull. Geol. Soc. Am. 120, 930–949. https://doi.org/10.1130/B26186.1

Mora, A., Horton, B.K., Mesa, A., Rubiano, J., Ketcham, R.A., Parra, M., Blanco, V., Garcia, D., Stockli, D.F., 2010a. Migration of Cenozoic deformation in the eastern cordillera of Colombia interpreted from fission track results and structural relationships: Implications for petroleum systems. Am. Assoc. Pet. Geol. Bull. 94, 1543–1580. https://doi.org/10.1306/01051009111

Mora, A., Parra, M., Strecker, M.R., Sobel, E.R., Zeilinger, G., Jaramillo, C., Da Silva, S.F., Blanco, M., 2010b. The eastern foothills of the Eastern Cordillera of Colombia: An example of multiple factors controlling structural styles and active tectonics. Bull. Geol. Soc. Am. 122, 1846–1864. https://doi.org/10.1130/B30033.1

Mora, A., Reyes-Harker, A., Rodriguez, G., Tesón, E., Ramirez-Arias, J.C., Parra, M., Caballero, V., Mora, J.P., Quintero, I., Valencia, V., Ibañez, M., Horton, B.K., Stockli, D.F., 2013. Inversion tectonics under increasing rates of shortening and sedimentation: Cenozoic example from the Eastern Cordillera of Colombia. Geol. Soc. London, Spec. Publ. 377, 411–442. https://doi.org/10.1144/SP377.6

Mora, A., Parra, M., Forero, G.R., Blanco, V., Moreno, N., Caballero, V., Stockli, D., Duddu, I., Ghorbal, B., 2015. What Drives Orogenic Asymmetry in the Northern Andes?: A Case Study from the Apex of the Northern Andean Orocline. Mem. 108 Pet. Geol. Potential Colomb. Caribb. Margin 547–586. https://doi.org/10.1306/13531949M1083652

Mora, A., García-Bautista, D.F., Reyes-Harker, A., Parra, M., Blanco, V., Sánchez, N., de La Parra, F., Caballero, V., Rodriguez, G., Ruiz, C., Naranjo, J., Tesón, E., Niño, F., Quintero, I., Moreno, N., Cardozo, E., Gamba, N., Horton, B.K., Arias-Martinez, J.P., 2019. Tectonic evolution of petroleum systems within the onshore Llanos Basin: Insights on the presence of Orinoco heavy oil analogs in Colombia and a comparison with other heavy oil provinces worldwide. Am. Assoc. Pet. Geol. Bull. 103, 1179–1224. https://doi.org/10.1306/1003181611417236

Moreno, N., Silva, A., Mora, A., Tesón, E., Quintero, I., Rojas, L.E., Lopez, C., Blanco, V., Castellanos, J., Sanchez, J., Osorio, L., Namson, J., Stockli, D., Casallas, W., 2013. Interaction between thin- and thick-skinned tectonics in the foothill areas of an inverted graben. The Middle Magdalena Foothill belt. Geol. Soc. London, Spec. Publ. 377, 221–255. https://doi.org/10.1144/SP377.8

Noriega-Londoño, S., Bermúdez, M.A., Marín-Cerón, M.I., Restrepo-Moreno, S., García-Delgado, H., 2021. Earthquake ground deformation using DInSAR analysis and instrumental seismicity: The 2019 M 6.0 Mesetas Earthquake, Meta, Colombia. Bol. Soc. Geol. Mex. A090221. http://dx.doi.org/10.18268/BSGM2021v73n2a090221

Ouimet, W.B., Whipple, K.X., Royden, L.H., Sun, Z., Chen, Z., 2007. The influence of large landslides on river incision in a transient landscape: Eastern margin of the Tibetan Plateau (Sichuan, China). Geol. Soc. Am. Bull. 119, 1462–1476. https://doi.org/10.1130/B26136.1

Ouimet, W.B., Whipple, K.X., Granger, D.E., 2009. Beyond threshold hillslopes: Channel adjustment to base-level fall in tectonically active mountain ranges. Geology 37, 579–582. https://doi.org/10.1130/G30013A.1

Parra, M., Mora, A., Jaramillo, C., Strecker, M.R., Sobel, E.R., Quiroz, L., Rueda, M., Torres, V., 2009a. Orogenic wedge advance in the northern Andes: Evidence from the Oligocene-Miocene sedimentary record of the Medina Basin, Eastern Cordillera, Colombia. Bull. Geol. Soc. Am. 121, 780–800. https://doi.org/10.1130/B26257.1

Parra, M., Mora, A., Sobel, E.R., Strecker, M.R., González, R., 2009b. Episodic orogenic front migration in the northern Andes: Constraints from low-temperature thermochronology in the Eastern Cordillera, Colombia. Tectonics 28. https://doi.org/10.1029/2008TC002423

Parra, M., Mora, A., Lopez, C., Rojas, L.E., Horton, B.K., 2012. Detecting earliest shortening and deformation advance in thrust belt hinterlands: Example from the Colombian Andes. Geology 40, 175–178. https://doi.org/10.1130/G32519.1

Pérez-Peña, J. V., Al-Awabdeh, M., Azañón, J.M., Galve, J.P., Booth-Rea, G., Notti, D., 2017. SwathProfiler and NProfiler: Two new ArcGIS Add-ins for the automatic extraction of swath and normalized river profiles. Comput. Geosci. 104, 135–150. https://doi.org/10.1016/j.cageo.2016.08.008

Pike, R.J., Wilson, S.E., 1971. Elevation-relief ratio, hypsometric integral, and geomorphic area-altitude analysis. Bull. Geol. Soc. Am. 82, 1079–1084. https://doi.org/10.1130/0016-7606(1971)82[1079:ERHIAG]2.0.CO;2

Ramirez-Arias, J., Mora, A., Parra, M., 2010. Indicadores sedimentológicos de la evolución tectónica durante el Mioceno en el Sinclinal de Nunchía, Piedemonte de la Cordillera Oriental de Colombia. Boletín Geol. 32, 29–44

Ramirez-Arias, J.C., Mora, A., Rubiano, J., Duddy, I., Parra, M., Moreno, N., Stockli, D., Casallas, W., 2012. The asymmetric evolution of the Colombian Eastern Cordillera. Tectonic inheritance or climatic forcing? New evidence from thermochronology and sedimentology. J. South Am. Earth Sci. 39, 112–137. https://doi.org/10.1016/j.jsames.2012.04.008

Reiners, P.W., Ehlers, T.A., Mitchell, S.G., Montgomery, D.R., 2003. Coupled spatial variations in rainfall and long-term erosion rates across the Washington Cascades. Nature 426, 645–647. https://doi.org/10.1038/nature02111

Reiners, P.W., and Brandon, M.T., 2006. Using Thermochronology To Understand Orogenic Erosion: Annual Review of Earth and Planetary Sciences 34, 419–466 https://doi.org/10.1146/annurev.earth.34.031405.125202.

Restrepo-Moreno, S.A., Foster, D.A., Bernet, M., Kohn, K., Noriega, S., 2019. Morphotectonic and orogenic development of the northern Andes of Colombia: A low-temperature thermochronology perspective, Frontiers in Earth Sciences. https://doi.org/10.1007/978-3-319-76132-9_11

Reyes-Harker, A., Ruiz-Valdivieso, C.F., Mora, A., Ramírez-Arias, J.C., Rodriguez, G., De La Parra, F., Caballero, V., Parra, M., Moreno, N., Horton, B.K., Saylor, J.E., Silva, A., Valencia, V., Stockli, D., Blanco, V., 2015. Cenozoic paleogeography of the Andean foreland and retroarc hinterland of Colombia, AAPG Bulletin https://doi.org/10.1306/06181411110

Rivière, J., Lv, Z., Johnson, P.A., Marone, C., 2018. Evolution of b-value during the seismic cycle: Insights from laboratory experiments on simulated faults. Earth Planet. Sci. Lett. 482, 407–413. https://doi.org/10.1016/j.epsl.2017.11.036

Roe, G.H., Montgomery, D.R., Hallet, B., 2002. Effects of orographic rainfall variations on the concavity of steady-state river profiles. Geology 30, 143–146. https://doi.org/10.1130/0091-7613(2002)030<0143:EOOPVO>2.0.CO;2

Roeder, D., Chamberlain, R.L., 1995. Eastern Cordillera of Colombia: Jurassic - Neogene crustal evolution. A.J. Tankard, R. Suarez S., H.J. Welsink, eds., Pet. basins South Am. AAPG Mem. 62 633–646. https://doi.org/10.1306/8D2B0C1A-171E-11D7-8645000102C1865D

Robert, X., Van Der Beek, P., Braun, J., Perry, C., Mugnier, J.L., 2011. Control of detachment geometry on

lateral variations in exhumation rates in the Himalaya: Insights from low-temperature thermochronology and numerical modeling. J. Geophys. Res. Solid Earth 116, 1–22. https://doi.org/10.1029/2010JB007893

Salcedo Hurtado, E., Rivera, C., Gómez Capera, A., 2001. Implicaciones sismotectónicas de las soluciones del mecanismo focal de algunos terremotos de la región central de Colombia. Geofísica Colomb. 18–26

Salles, T., Rey, P., Bertuzzo, E., 2019. Mapping landscape connectivity as a driver of species richness under tectonic and climatic forcing. Earth Surf. Dyn. 7, 895–910. https://doi.org/10.5194/esurf-7-895-2019

Sánchez, J., Horton, B.K., Tesón, E., Mora, A., Ketcham, R.A., Stockli, D.F., 2012. Kinematic evolution of Andean fold-thrust structures along the boundary between the Eastern Cordillera and Middle Magdalena Valley basin, Colombia. Tectonics 31, 1–24. https://doi.org/10.1029/2011TC003089

Sarmiento-Rojas, L.F.F., Van Wess, J.D.D., Cloetingh, S., 2006. Mesozoic transtensional basin history of the Eastern Cordillera, Colombian Andes: Inferences from tectonic models. J. South Am. Earth Sci. 21, 383–411. https://doi.org/10.1016/j.jsames.2006.07.003

Sarmiento, G., Gaviria, S., Hooghiemstra, H., Berrio, J.C., van der Hammen, T., 2008. Landscape evolution and origin of Lake Fúquene (Colombia): Tectonics, erosion and sedimentation processes during the Pleistocene. Geomorphology 100, 563–575. https://doi.org/10.1016/j.geomorph.2008.02.006

Saylor, J.E., Horton, B.K., Stockli, D.F., Mora, A., and Corredor, J., 2012a. Structural and thermochronological evidence for Paleogene basement-involved shortening in the axial Eastern Cordillera, Colombia: Journal of South American Earth Sciences 39. 202–215. https://doi.org/10.1016/j.jsames.2012.04.009.

Saylor, J.E., Stockli, D.F., Horton, B.K., Nie, J., Mora, A., 2012b. Discriminating rapid exhumation from syndepositional volcanism using detrital zircon double dating: Implications for the tectonic history of the Eastern Cordillera, Colombia. Bull. Geol. Soc. Am. 124, 762–779. https://doi.org/10.1130/B30534.1

Schildgen, T.F., Van Der Beek, P.A., Sinclair, H.D., Thiede, R.C., 2018. Spatial correlation bias in late-Cenozoic erosion histories derived from thermochronology. Nature 559, 89–93. https://doi.org/10.1038/s41586-018-0260-6

Schorlemmer, D., Wiemer, S., Wyss, M., 2005. Variations in earthquake-size distribution across different stress regimes. Nature 437, 539–542. https://doi.org/10.1038/nature04094

Schwanghart, W., Scherler, D., 2014. Short Communication: TopoToolbox 2 - MATLAB-based software for topographic analysis and modeling in Earth surface sciences. Earth Surf. Dyn. 2, 1–7. https://doi.org/10.5194/esurf-2-1-2014

Scotti, V.N., Molin, P., Faccenna, C., Soligo, M., Casas-Sainz, A., 2014. The influence of surface and tectonic

processes on landscape evolution of the Iberian Chain (Spain): Quantitative geomorphological analysis and geochronology. Geomorphology 206, 37–57. https://doi.org/10.1016/j.geomorph.2013.09.017

Seagren, E.G., Schoenbohm, L.M., 2019. Base Level and Lithologic Control of Drainage Reorganization in the Sierra de las Planchadas, NW Argentina. J. Geophys. Res. Earth Surf. 124, 1516–1539. https://doi.org/10.1029/2018JF004885

Shagam, R., Kohn, B.P., Banks, P.O., Dasch, L.E., Vargas, R., Pimentel, N., 1984. Tectonic implications of Cretaceous-Pliocene fission track ages from rocks of the circum-Maracaibo basin of western Venezuela and eastern Colombia. Caribbean-South Am. Plate Bound. Reg. Tectonics 162, 385–412. https://doi.org/10.1130/MEM162

Silva, A., Mora, A., Caballero, V., Rodriguez, G., Ruiz, C., Moreno, N., Parra, M., Ramirez-Arias, J.C., Ibáñez, M., Quintero, I., 2013. Basin compartmentalization and drainage evolution during rift inversion: evidence from the Eastern Cordillera of Colombia. Geol. Soc. London, Spec. Publ. 377, 369–409. https://doi.org/10.1144/SP377.15

Siravo, G., Fellin, M.G., Faccenna, C., Bayona, G., Lucci, F., Molin, P., Maden, C., 2018. Constraints on the Cenozoic deformation of the northern Eastern Cordillera, Colombia. Tectonics. https://doi.org/10.1029/2018TC005162

Siravo, G., Fellin, M.G., Faccenna, C., Maden, C., Gaia, S., Fellin, M.G., Faccenna, C., Maden, C., 2019a. Transpression and the build-up of the Cordillera: the example of the Bucaramanga fault (Eastern Cordillera, Colombia). J. Geol. Soc. London. 13, jgs2019-054. https://doi.org/10.1144/jgs2019-054

Siravo, G., Faccenna, C., Gérault, M., Becker, T.W., Fellin, M.G., Herman, F., Molin, P., 2019b. Slab flattening and the rise of the Eastern Cordillera, Colombia. Earth Planet. Sci. Lett. 512, 100–110. https://doi.org/10.1016/j.epsl.2019.02.002

Smith, W.D., 1981. The b-value as an earthquake precursor. Nature 289, 136–139. https://doi.org/10.1038/289136a0

Stolar, D., Roe, G., Willett, S., 2007. Controls on the patterns of topography and erosion rate in a critical orogen. J. Geophys. Res. Earth Surf. 112, 1–17. https://doi.org/10.1029/2006JF000713

Strahler, A.N., 1952. Hypsometric (area-altitude) analysis of erosional topography. GSA Bull. 63, 1117–1142.

Struth, L., Teixell, A., Owen, L.A., Babault, J., 2016. Plateau reduction by drainage divide migration in the Eastern Cordillera of Colombia defined by morphometry and10Be terrestrial cosmogenic nuclides. Earth Surf. Process. Landforms 42, 1155–1170. https://doi.org/10.1002/esp.4079

Telbisz, T., Kovács, G., Székely, B., Szabó, J., 2013. Topographic swath profile analysis: a generalization and sensitivity evaluation of a digital terrain analysis tool. Zeitschrift für Geomorphol. 57, 485–513.

https://doi.org/10.1127/0372-8854/2013/0110

Taboada, A., Rivera, L., Fuenzalida, A., Cisternas, A., Philip, H., Bijwaard, H., Olaya, J., Rivera, C., 2000. Geodynamics of the northern Andes: subductions and intracontinental deformation (Colombia). Tectonics 19 (5), 787–813.

Tesón, E., Mora, A., Silva, A., Namson, J., Teixell, A., Castellanos, J., Casallas, W., Julivert, M., Taylor, M., Ibáñez-Mejía, M., Valencia, V.A., 2013. Relationship of Mesozoic graben development, stress, shortening magnitude, and structural style in the Eastern Cordillera of the Colombian Andes. Geol. Soc. London, Spec. Publ. 377, 257–283. https://doi.org/10.1144/SP377.10

Torres, V., Vandenberghe, J., Hooghiemstra, H., 2005. An environmental reconstruction of the sediment infill of the Bogotá basin (Colombia) during the last 3 million years from abiotic and biotic proxies. Palaeogeogr. Palaeoclimatol. Palaeoecol. 226, 127–148. https://doi.org/10.1016/j.palaeo.2005.05.005

Trenkamp, R., Kellogg, J.N., Freymueller, J.T., Mora, H.P., 2002. Wide plate margin deformation, southern Central America and northwestern South America, CASA GPS observations. J. South Am. Earth Sci. 15, 157–171. https://doi.org/10.1016/S0895-9811(02)00018-4

Ujueta, G., 2014. Tectónica de Bloques, delimitados por lineamientos NNE-SSO y NO-SE, en Colombia. Geología Colombiana 39, 37-54.

van der Beek, P., Litty, C., Baudin, M., Mercier, J., Robert, X., Hardwick, E., 2016. Contrasting tectonically driven exhumation and incision patterns, western versus central Nepal Himalaya. Geology 44, 327–330. https://doi.org/10.1130/G37579.1

van der Hammen, T., 1974. The Pleistocene Changes of Vegetation and Climate in Tropical South America. J. Biogeogr. 1, 3. https://doi.org/10.2307/3038066

van der Hammen, T., Cleef, A., 1992. Holocene changes of rainfall and river discharge in Northern South America and the El Niño phenomenon. Erdkunde 46, 252–256

van der Hammen, T., Hooghiemstra, H., 1996. The El Abra Estadial, a younger dryas equivalent in Colombia. Quat. Sci. Rev. 14, 841–851

van der Hammen, T., Hooghiemstra, H., 2000. Neogene and Quaternary history of vegetation, climate, and plant diversity in Amazonia. Quat. Sci. Rev. 19, 725–742. https://doi.org/10.1097/MD.0000000000004157

van der Hammen, T., Hooghiemstra, H., 2003. Interglacial-glacial Fuquene-3 pollen record from Colombia: An Eemian to Holocene climate record. Glob. Planet. Change 36, 181–199. https://doi.org/10.1016/S0921-8181(02)00184-4

van der Lelij, R., Spikings, R., Mora, A., 2016. Thermochronology and tectonics of the Mérida Andes and the

Santander Massif, NW South America. Lithos 248–251, 220–239. https://doi.org/10.1016/j.lithos.2016.01.006

Vargas, C.A., 2020. Subduction Geometries in Northwestern South America, in: Gómez, J., Pinilla-Pachón, A.O. (Eds.), The Geology of Colombia. Servicio Geológico Colombiano, pp. 1–26. https://doi.org/10.32685/pub.esp.38.2019.11

Vargas, C.A.C.A., Mann, P., 2013. Tearing and breaking off of subducted slabs as the result of collision of the panama arc-indenter with Northwestern South America. Bull. Seismol. Soc. Am. 103, 2025–2046. https://doi.org/10.1785/0120120328

Velandia, F., De Bermoudes, O., 2002. Fallas longitudinales y transversales de la Sabana de Bogotá, Colombia. Bol. Geol. 24 (39), 37–48.

Velandia, F., 2005. Interpretación de transcurrencia de las fallas Soapaga y Boyacá a partir de Imágenes LANDSAT TM. Bol. Geol. 27 (1), 81–94.

Velandia, F., Bermúdez, M.A., 2018. The transpressive southern termination of the Bucaramanga fault (Colombia): insights from geological mapping, stress tensors, and fractal analysis. J. Struct. Geol. 115, 190–207. https://doi.org/10.1016/J.JSG.2018.07.020

Velandia, F., García-Delgado, H., Zuluaga, C.A., López, J.A., Bermúdez, M.A., Audemard, F.A., 2020. Present-day structural frame of the Santander Massif and Pamplona Wedge: The interaction of the Northern Andes. Journal of Structural Geology, 137, https://doi.org/10.1016/J.JSG.2020.104087

Veloza, G., Taylor, M., Mora, A., Gosse, J., 2015. Active mountain building along the eastern Colombian Subandes: A folding history from deformed terraces across the Tame anticline, Llanos Basin. Bull. Geol. Soc. Am. 127, 1155–1173. https://doi.org/10.1130/B31168.1

Venables, W.N., Ripley, B.D., 2002. Modern Applied Statistics with S. 4th edition, Springer-Verlag New York.

Vernon, A.J., van der Beek, P.A., Sinclair, H.D., 2009. Spatial correlation between long-term exhumation rates and present-day forcing parameters in the western European Alps. Geology 37, 859–862. https://doi.org/10.1130/G25740A.1

Wang, P., Scherler, D., Liu-Zeng, J., Mey, J., Avouac, J.P., Zhang, Y., Shi, D., 2014. Tectonic control of Yarlung Tsangpo Gorge revealed by a buried canyon in Southern Tibet. Science 346, 978–981. https://doi.org/10.1126/science.1259041

Whipple, K.X., 2001. Fluvial landscape response time: How plausible is steady-state denudation? Am. J. Sci. 301, 313–325. https://doi.org/10.2475/ajs.301.4-5.313

Whipple, K.X., 2004. Bedrock Rivers and the Geomorphology of Active Orogens. Annu. Rev. Earth

Planet. Sci. 32, 151–185. https://doi.org/10.1146/annurev.earth.32.101802.120356

Whipple, K.X., 2009. The influence of climate on the tectonic evolution of mountain belts. Nat. Geosci. 2, 97–104. https://doi.org/10.1038/ngeo413

Whipple, K.X., Tucker, G.E., 1999. Dynamics of the stream-power river incision model: Implications for height limits of mountain ranges, landscape response timescales, and research needs. J. Geophys. Res. Solid Earth 104, 17661–17674. https://doi.org/10.1029/1999JB900120

Whipple, K.X., DiBiase, R.A., Crosby, B.T., 2013. Bedrock Rivers, Treatise on Geomorphology. Elsevier Ltd. https://doi.org/10.1016/B978-0-12-374739-6.00254-2

Whipple, K.X., Gasparini, N.M., 2014. Tectonic control of topography, rainfall patterns, and erosion during rapid post-12 Ma uplift of the Bolivian Andes. Lithosphere 6, 251–268. https://doi.org/10.1130/L325.1

Whipple, K.X., DiBiase, R.A., Ouimet, W.B., Forte, A.M., 2017. Preservation or piracy: Diagnosing low-relief, high-elevation surface formation mechanisms. Geology 45, 91–94. https://doi.org/10.1130/G38490.1

Whittaker, A.C., Boulton, S.J., 2012. Tectonic and climatic controls on knickpoint retreat rates and landscape response times. J. Geophys. Res. Earth Surf. 117, 1–19. https://doi.org/10.1029/2011JF002157

Wijninga, V.M., 1996. Neogene ecology of the Salto de Tequendama site (2475 m altitude, Cordillera Oriental, Colombia): The paleobotanical record of montane and lowland forests. Rev. Palaeobot. Palynol. 92, 97–156. https://doi.org/10.1016/0034-6667(94)00100-6

Willett, S., 1999. Orogeny and orography: The effects of erosion on the structure of mountain belts. J. Geophys. Res. Earth Surf. 104, 28957–28981. https://doi.org/https://doi.org/10.1029/1999JB900248

Willett, S.D., Herman, F., Fox, M., Stalder, N., Ehlers, T.A., Jiao, R., Yang, R., 2020. Bias and error in modelling thermochronometric data: resolving a potential increase in Plio-Pleistocene erosion rate. Earth Surf. Dyn. Discussion. https://doi.org/https://doi.org/10.5194/esurf-2020-59

Wobus, C., Whipple, K.X., Kirby, E., Snyder, N., Johnson, J., Spyropolou, K., Crosby, B., Sheehan, D., 2006. Tectonics from topography: Procedures, promise, and pitfalls, in: Special Paper 398: Tectonics, Climate, and Landscape Evolution. Geological Society of America, pp. 55–74. https://doi.org/10.1130/2006.2398(04)

Wu, Y.M., Chen, S.K., Huang, T.C., Huang, H.H., Chao, W.A., Koulakov, I., 2018. Relationship Between Earthquake b-Values and Crustal Stresses in a Young Orogenic Belt. Geophys. Res. Lett. 45, 1832–1837. https://doi.org/10.1002/2017GL076694

Highlights

- Drivers of the denudation rates for the Colombian Eastern Cordillera are studied
- The climate vs tectonics hypotheses are tested through statistical analysis
- Long to short-term erosion rates are controlled by tectonic inheritance
- Climate only plays a local role in short-term erosion rates

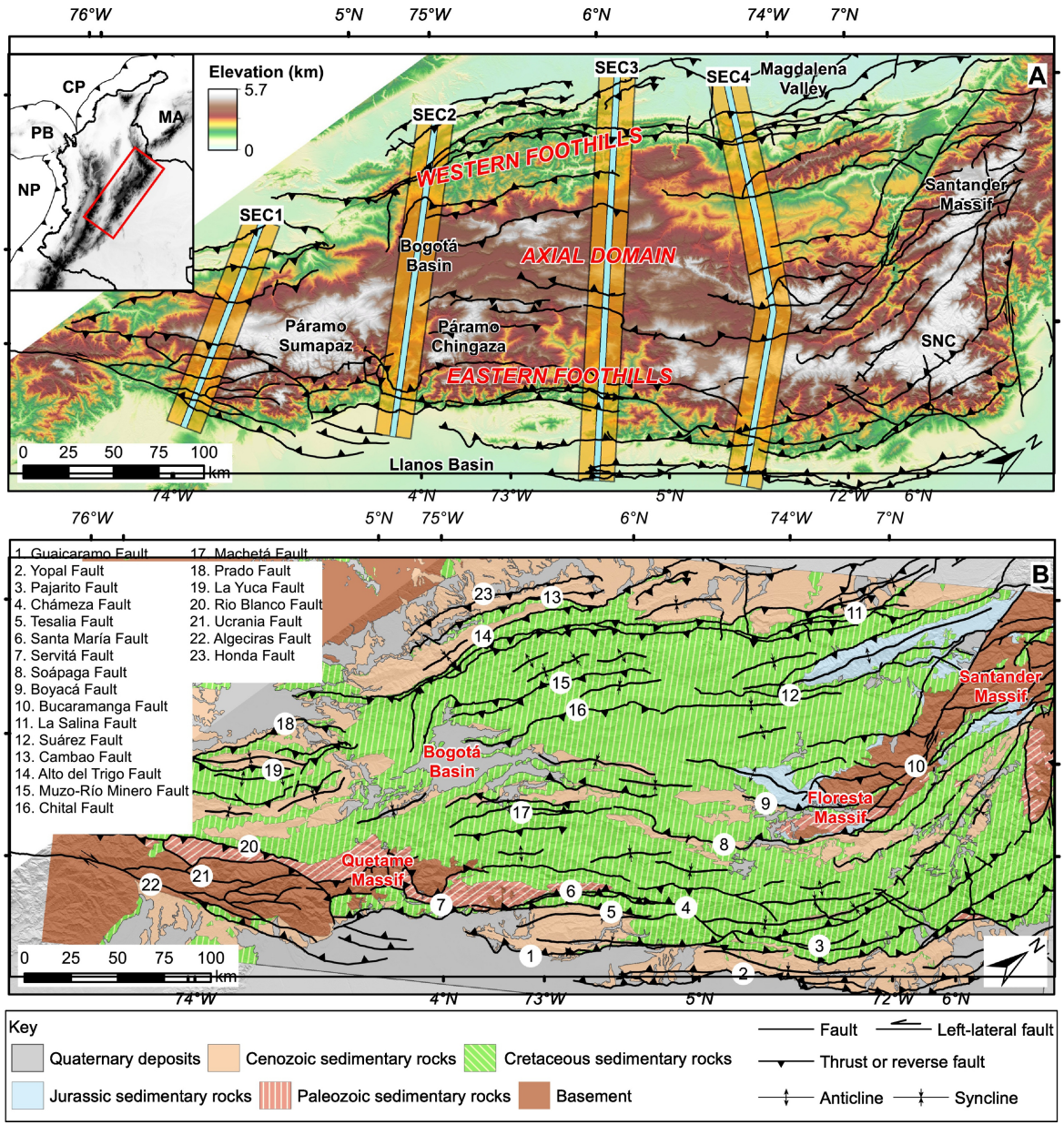
A
B
CP
MA
PB
NP
Elevation (km)
5.7
0
SEC1
SEC2
SEC3
SEC4
Magdalena Valley
WESTERN FOOTHILLS
AXIAL DOMAIN
EASTERN FOOTHILLS
Bogotá Basin
Páramo Sumapaz
Páramo Chingaza
Santander Massif
SNC
Llanos Basin
Floresta Massif
Quetame Massif
0 25 50 75 100 km
1. Guaicaramo Fault
2. Yopal Fault
3. Pajarito Fault
4. Chámeza Fault
5. Tesalia Fault
6. Santa María Fault
7. Servitá Fault
8. Soápaga Fault
9. Boyacá Fault
10. Bucaramanga Fault
11. La Salina Fault
12. Suárez Fault
13. Cambao Fault
14. Alto del Trigo Fault
15. Muzo-Río Minero Fault
16. Chital Fault
17. Machetá Fault
18. Prado Fault
19. La Yuca Fault
20. Rio Blanco Fault
21. Ucrania Fault
22. Algeciras Fault
23. Honda Fault
Key
Quaternary deposits
Cenozoic sedimentary rocks
Cretaceous sedimentary rocks
Jurassic sedimentary rocks
Paleozoic sedimentary rocks
Basement
Fault
Left-lateral fault
Thrust or reverse fault
Anticline
Syncline

Figure 1

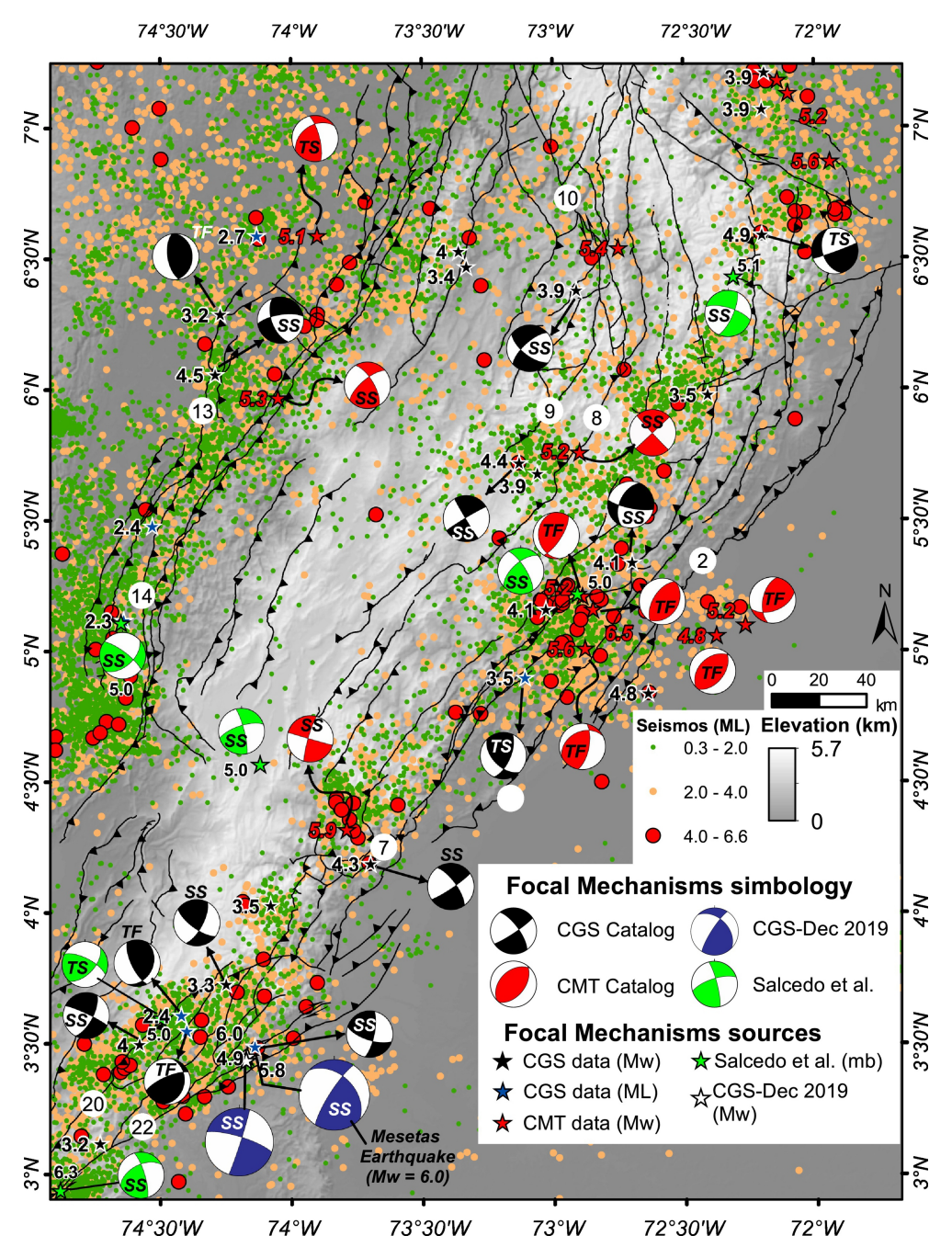
74°30'W
74°W
73°30'W
73°W
72°30'W
72°W
7°N
6°30'N
6°N
5°30'N
5°N
4°30'N
4°N
3°30'N
3°N
N
0 20 40
km
Seismos (ML)
0.3 - 2.0
2.0 - 4.0
4.0 - 6.6
Elevation (km)
5.7
0
Focal Mechanisms simbology
CGS Catalog
CGS-Dec 2019
CMT Catalog
Salcedo et al.
Focal Mechanisms sources
CGS data (Mw)
Salcedo et al. (mb)
CGS data (ML)
CGS-Dec 2019 (Mw)
CMT data (Mw)
Mesetas Earthquake (Mw = 6.0)

Figure 2

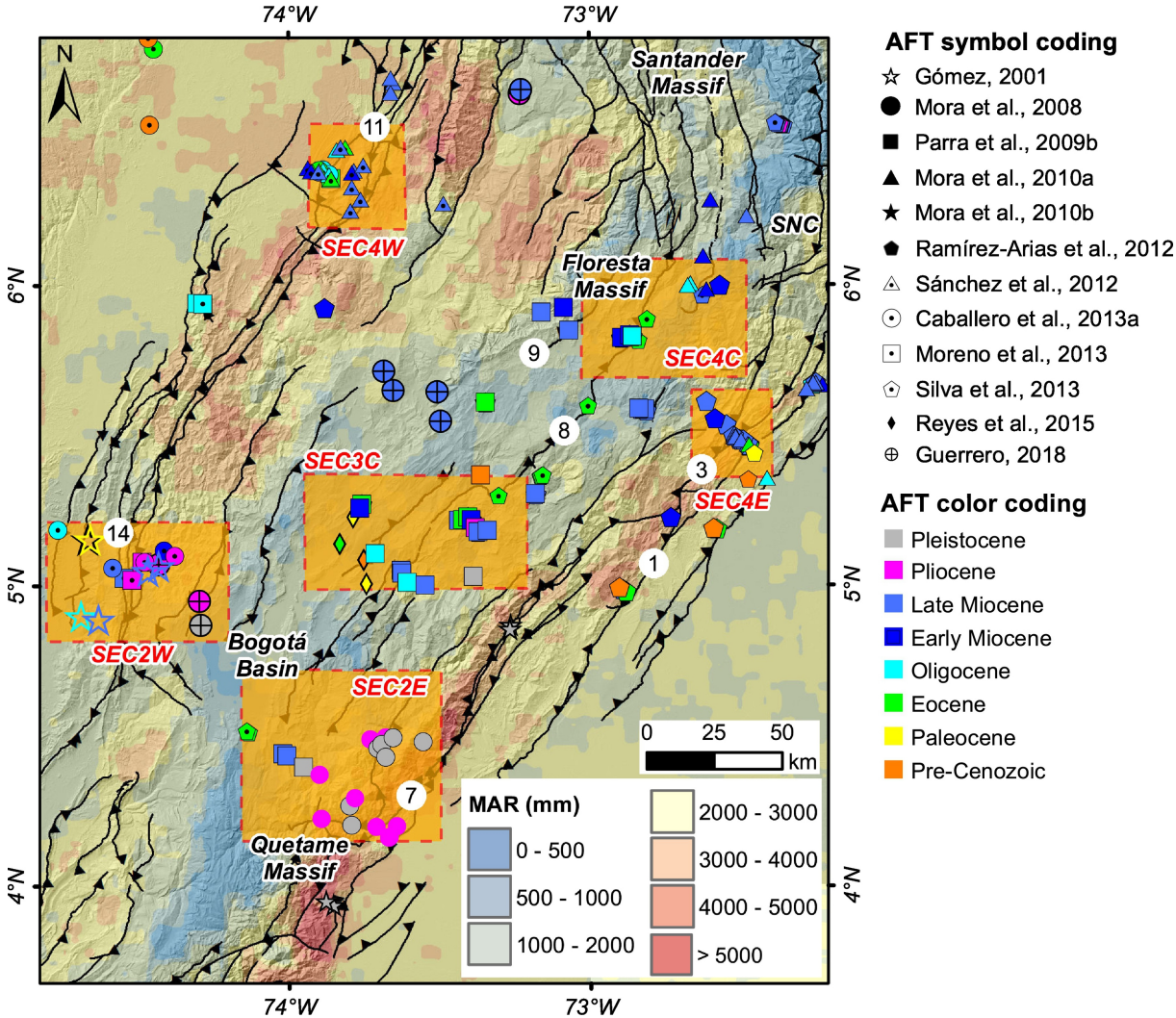
74°W
73°W
N
6°N
5°N
4°N
Santander Massif
SNC
Floresta Massif
SEC4W
SEC4C
SEC4E
SEC3C
SEC2W
SEC2E
Bogotá Basin
Quetame Massif
11
9
8
3
14
1
7
0 25 50
km
MAR (mm)
0 - 500
500 - 1000
1000 - 2000
2000 - 3000
3000 - 4000
4000 - 5000
> 5000
AFT symbol coding
Gómez, 2001
Mora et al., 2008
Parra et al., 2009b
Mora et al., 2010a
Mora et al., 2010b
Ramírez-Arias et al., 2012
Sánchez et al., 2012
Caballero et al., 2013a
Moreno et al., 2013
Silva et al., 2013
Reyes et al., 2015
Guerrero, 2018
AFT color coding
Pleistocene
Pliocene
Late Miocene
Early Miocene
Oligocene
Eocene
Paleocene
Pre-Cenozoic

Figure 3

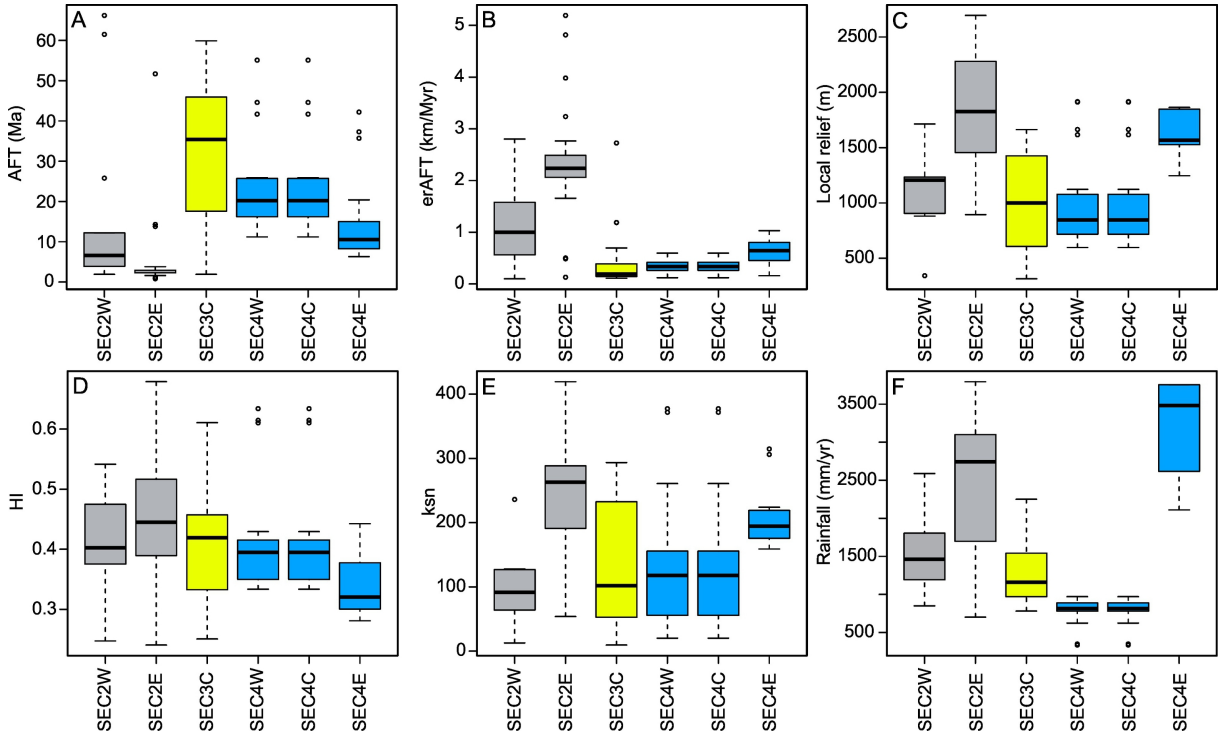
A
AFT (Ma)
0
10
20
30
40
50
60
B
erAFT (km/Myr)
0
1
2
3
4
5
C
Local relief (m)
500
1000
1500
2000
2500
D
HI
0.3
0.4
0.5
0.6
E
ksn
0
100
200
300
400
F
Rainfall (mm/yr)
500
1500
2500
3500
SEC2W
SEC2E
SEC3C
SEC4W
SEC4C
SEC4E

Figure 4

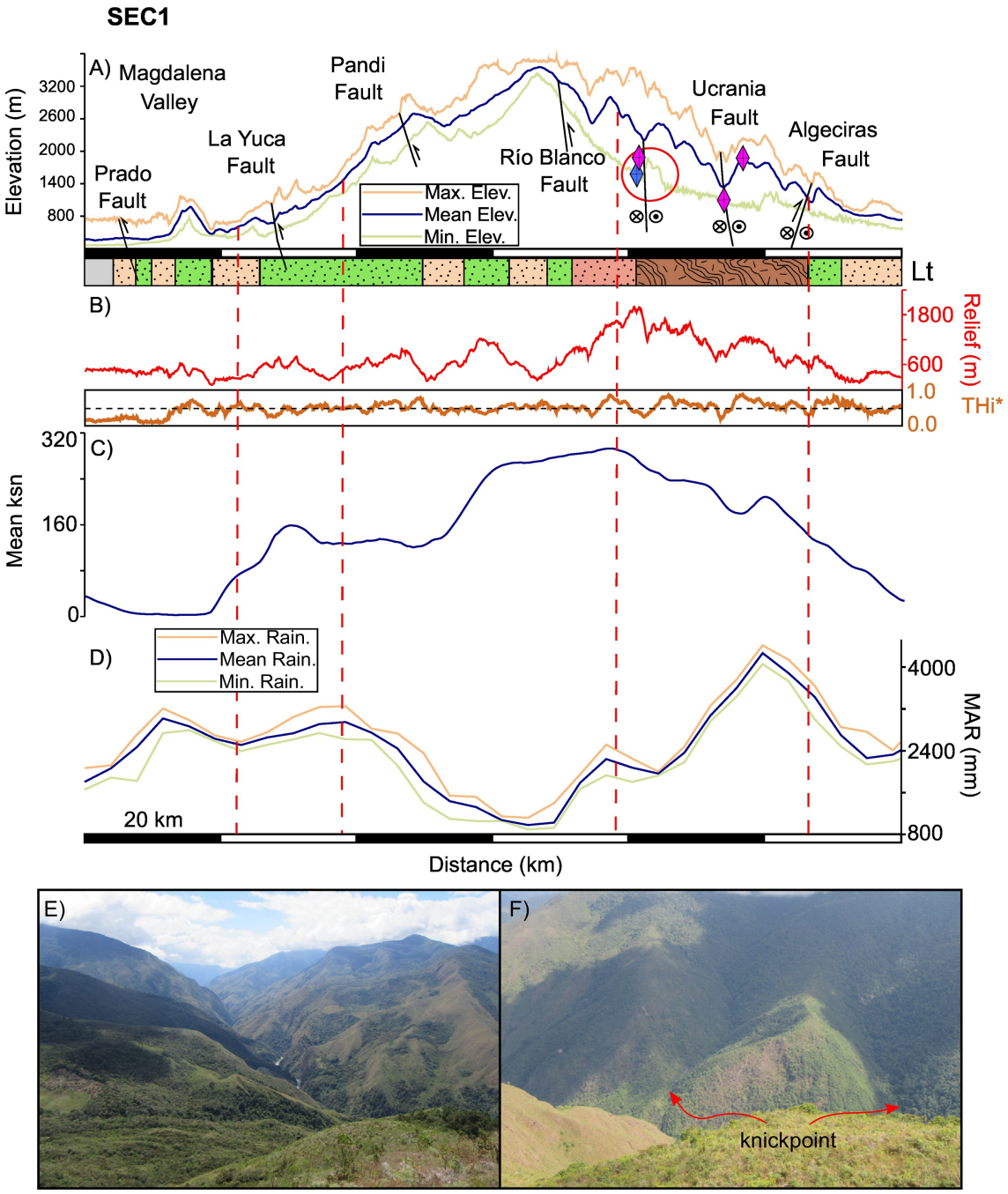
SEC1
A)
Magdalena Valley
Prado Fault
La Yuca Fault
Pandi Fault
Río Blanco Fault
Ucrania Fault
Algeciras Fault
Elevation (m)
3200
2600
2000
1400
800
Max. Elev.
Mean Elev.
Min. Elev.
Lt
B)
1800
600
Relief (m)
1.0
0.0
THi*
C)
Mean ksn
320
160
0
D)
Max. Rain.
Mean Rain.
Min. Rain.
4000
2400
800
MAR (mm)
20 km
Distance (km)
E)
F)
knickpoint

Figure 5

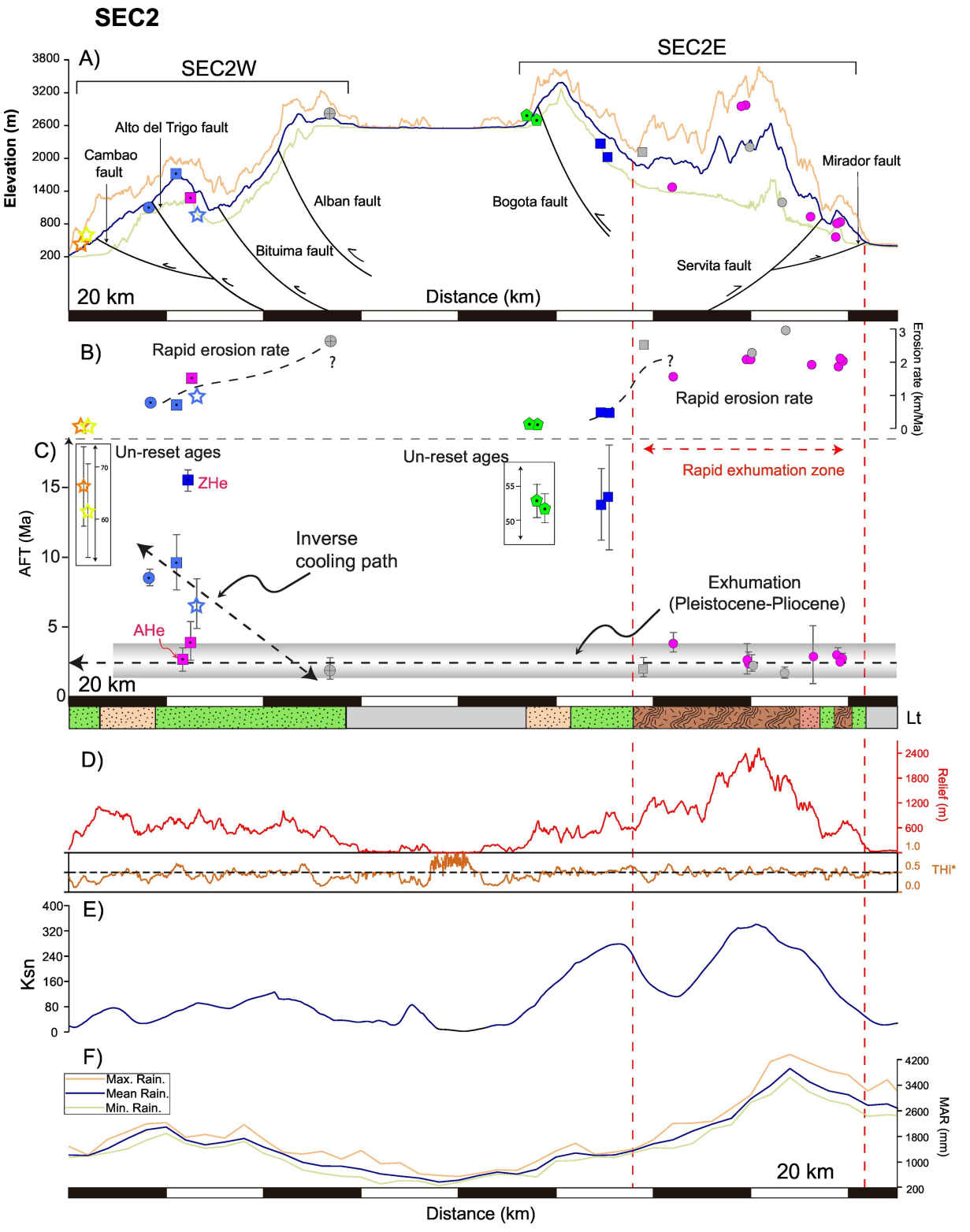
SEC2
A)
SEC2W
SEC2E
Elevation (m)
3800
3200
2600
2000
1400
800
200
Alto del Trigo fault
Cambao fault
Alban fault
Bituima fault
Bogota fault
Mirador fault
Servita fault
20 km
Distance (km)
B)
Rapid erosion rate
?
Rapid erosion rate
Erosion rate (km/Ma)
3
2
1
0
C)
Un-reset ages
ZHe
Un-reset ages
Rapid exhumation zone
AFT (Ma)
15
10
5
0
Inverse cooling path
Exhumation (Pleistocene-Pliocene)
AHe
20 km
Lt
D)
Relief (m)
2400
1800
1200
600
1.0
0.5
0.0
THi*
E)
Ksn
400
320
240
160
80
0
F)
Max. Rain.
Mean Rain.
Min. Rain.
MAR (mm)
4200
3400
2600
1800
1000
200
20 km
Distance (km)

Figure 6

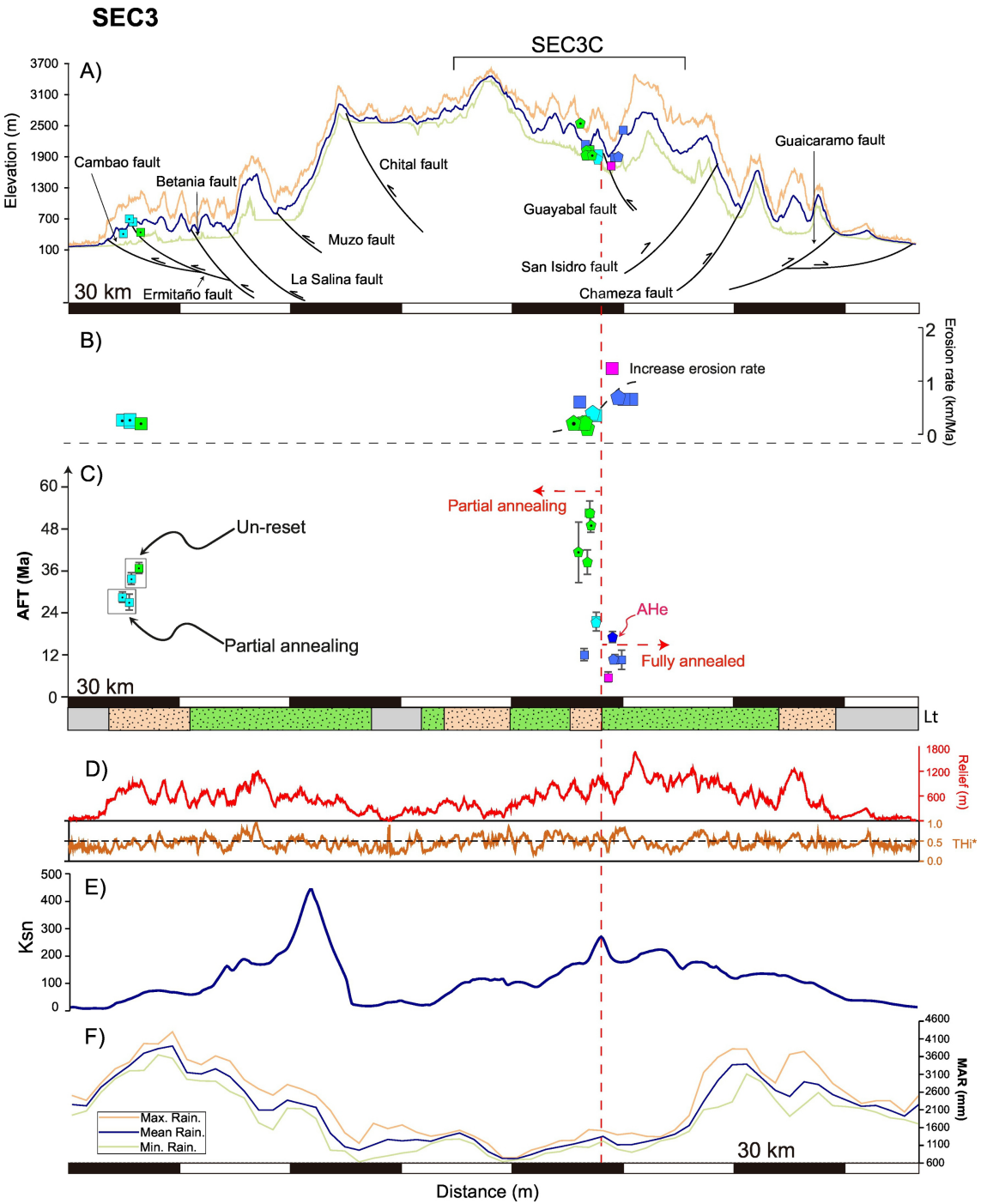
SEC3
SEC3C
A)
Elevation (m)
3700
3100
2500
1900
1300
700
100
Cambao fault
Betania fault
Chital fault
Guayabal fault
Guaicaramo fault
Muzo fault
La Salina fault
San Isidro fault
Ermitaño fault
Chameza fault
30 km
B)
Increase erosion rate
Erosion rate (km/Ma)
2
1
0
C)
AFT (Ma)
60
48
36
24
12
0
Un-reset
Partial annealing
Partial annealing
AHe
Fully annealed
30 km
Lt
D)
Relief (m)
1800
1200
600
THi*
1.0
0.5
0.0
E)
Ksn
500
400
300
200
100
0
F)
MAR (mm)
4600
4100
3600
3100
2600
2100
1600
1100
600
Max. Rain.
Mean Rain.
Min. Rain.
30 km
Distance (m)

Figure 7

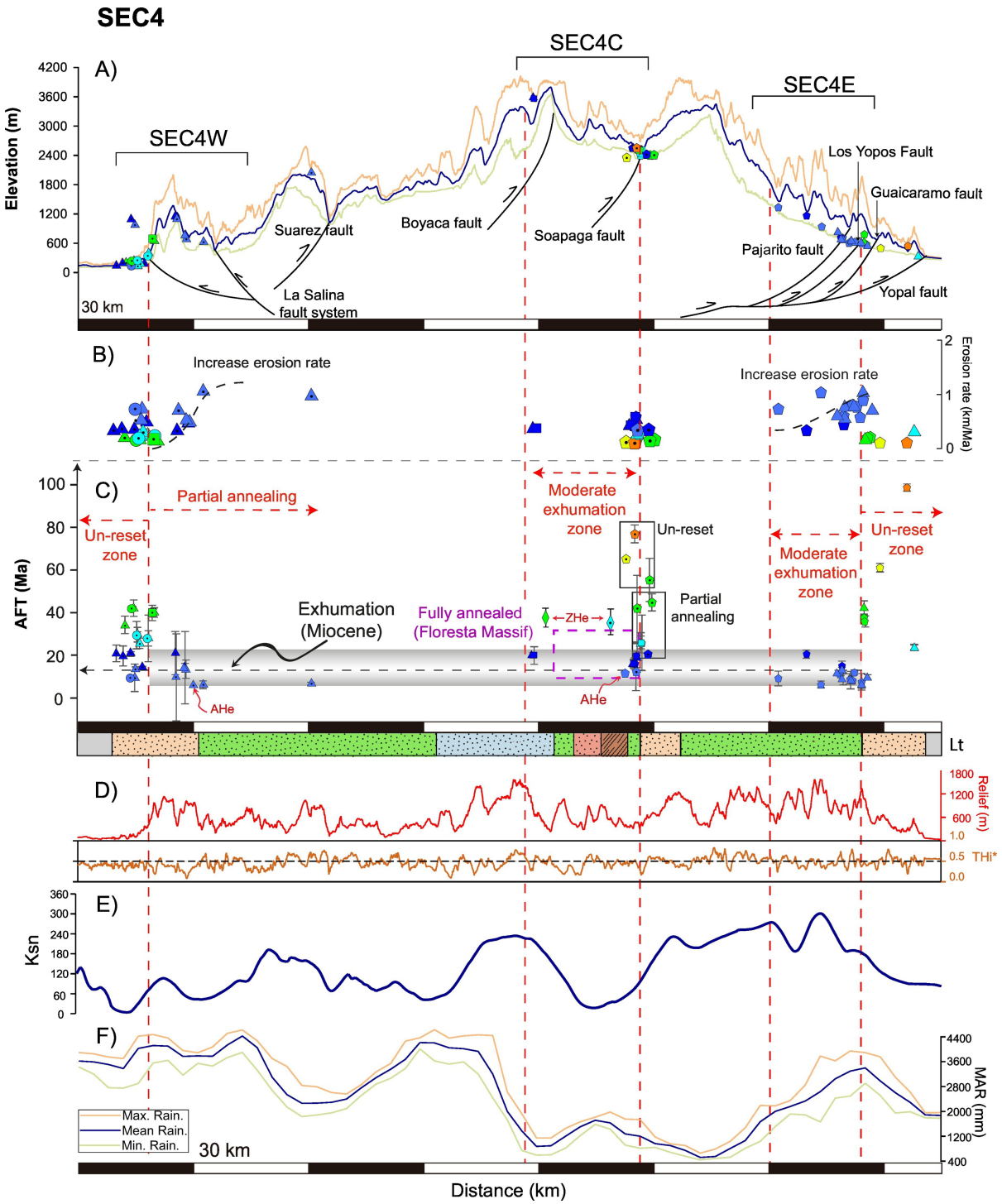
SEC4
SEC4C
SEC4E
SEC4W
A)
Elevation (m)
4200
3600
3000
2400
1800
1200
600
0
30 km
Suarez fault
La Salina
fault system
Boyaca fault
Soapaga fault
Los Yopos Fault
Guaicaramo fault
Pajarito fault
Yopal fault
B)
Increase erosion rate
Increase erosion rate
Erosion rate (km/Ma)
2
1
0
C)
AFT (Ma)
100
80
60
40
20
0
Partial annealing
Un-reset
zone
Moderate
exhumation
zone
Un-reset
Un-reset
zone
Moderate
exhumation
zone
Exhumation
(Miocene)
Fully annealed
(Floresta Massif)
←ZHe→
Partial
annealing
AHe
AHe
Lt
D)
Relief (m)
1800
1200
600
1.0
THi*
0.5
0.0
E)
Ksn
360
300
240
180
120
60
0
F)
MAR (mm)
4400
3600
2800
2000
1200
400
Max. Rain.
Mean Rain.
Min. Rain.
30 km
Distance (km)

Figure 8

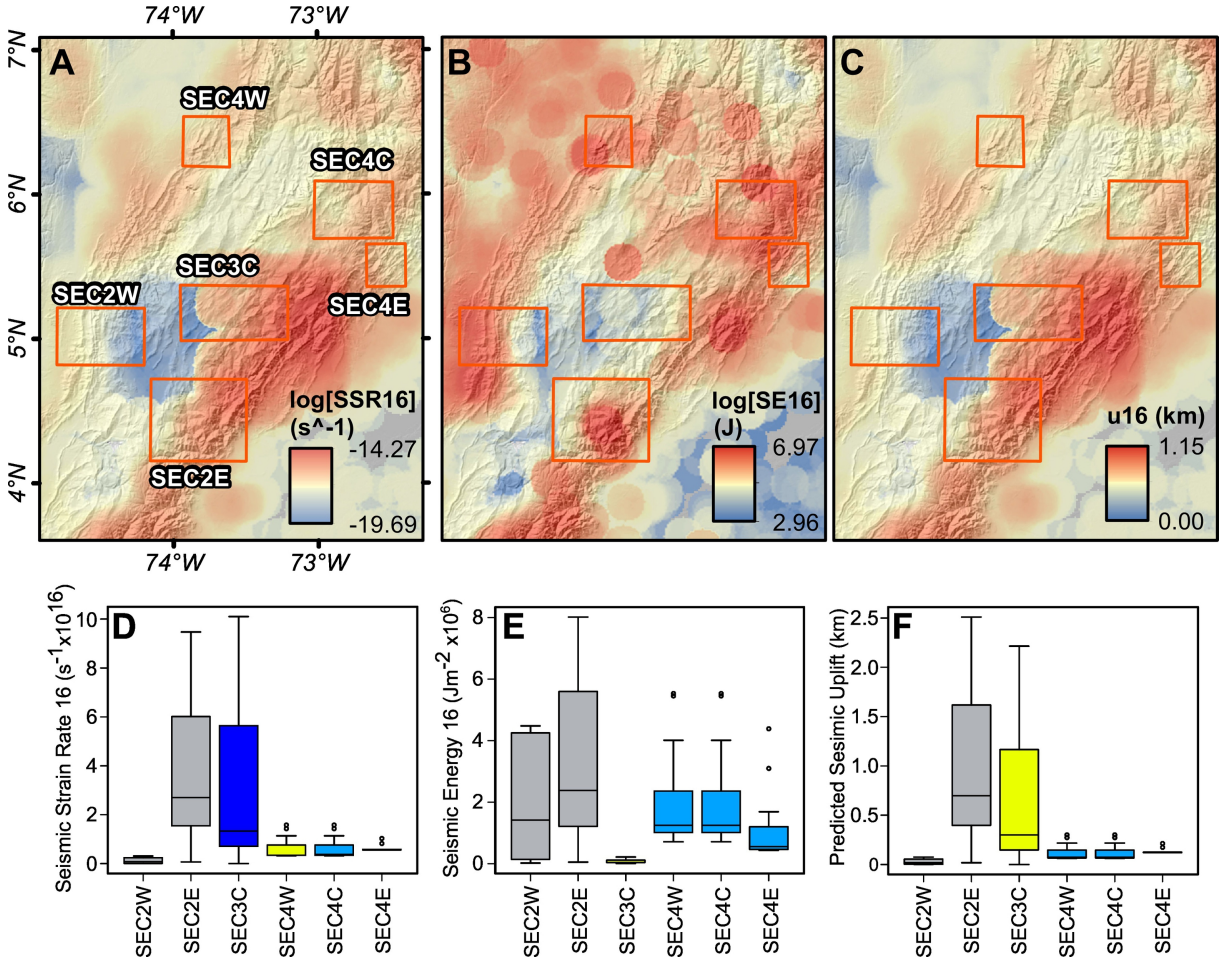
74°W
73°W
7°N
6°N
5°N
4°N
A
B
C
SEC4W
SEC4C
SEC3C
SEC2W
SEC4E
SEC2E
log[SSR16]
(s^-1)
-14.27
-19.69
log[SE16]
(J)
6.97
2.96
u16 (km)
1.15
0.00
D
Seismic Strain Rate 16 (s-1x10-16)
E
Seismic Energy 16 (Jm-2 x106)
F
Predicted Sesimic Uplift (km)
SEC2W
SEC2E
SEC3C
SEC4W
SEC4C
SEC4E

Figure 9

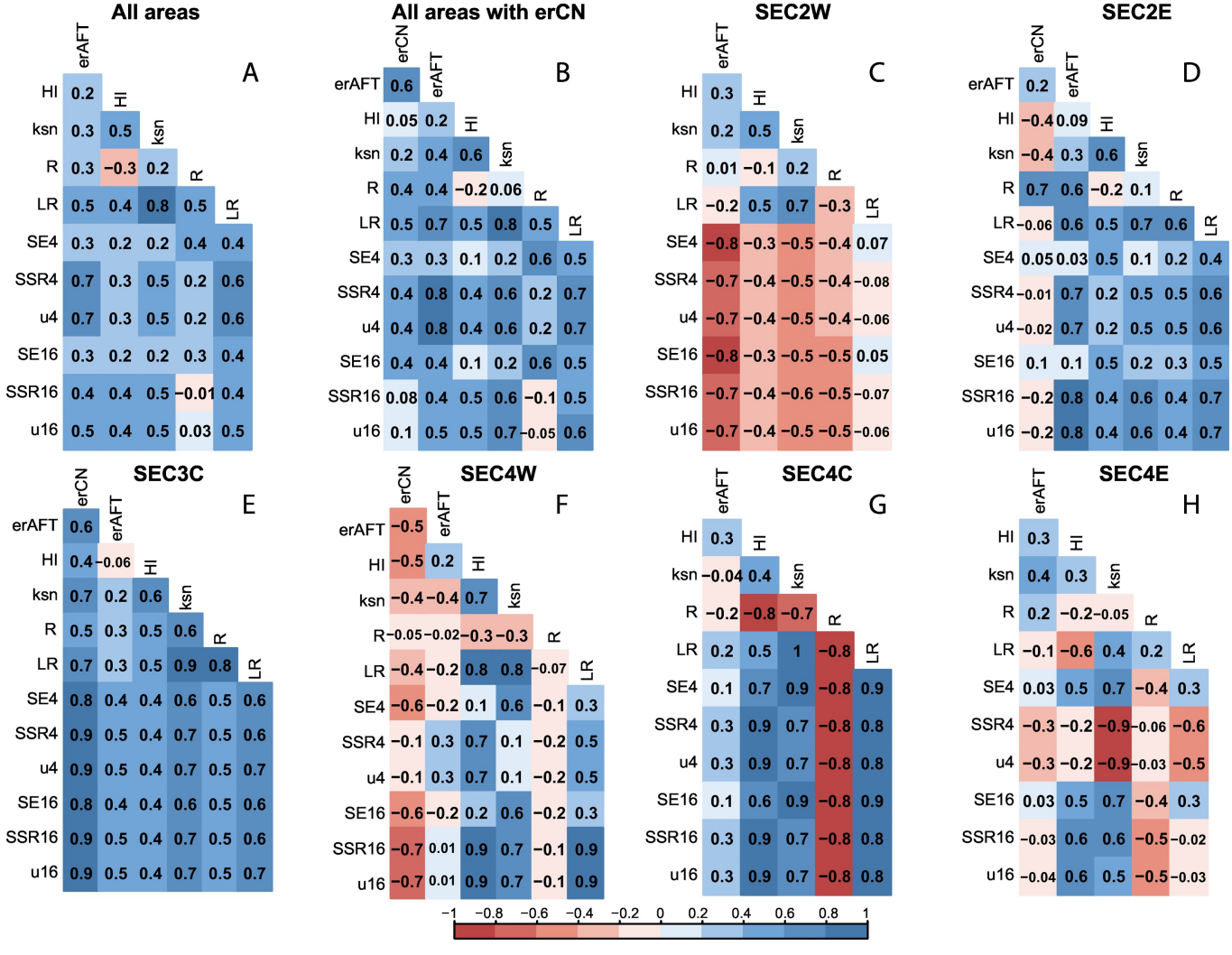
All areas
A
erAFT
HI
ksn
R
LR
SE4
SSR4
u4
SE16
SSR16
u16
All areas with erCN
B
erCN
SEC2W
C
SEC2E
D
SEC3C
E
SEC4W
F
SEC4C
G
SEC4E
H
−1
−0.8
−0.6
−0.4
−0.2
0
0.2
0.4
0.6
0.8
1

Figure 10

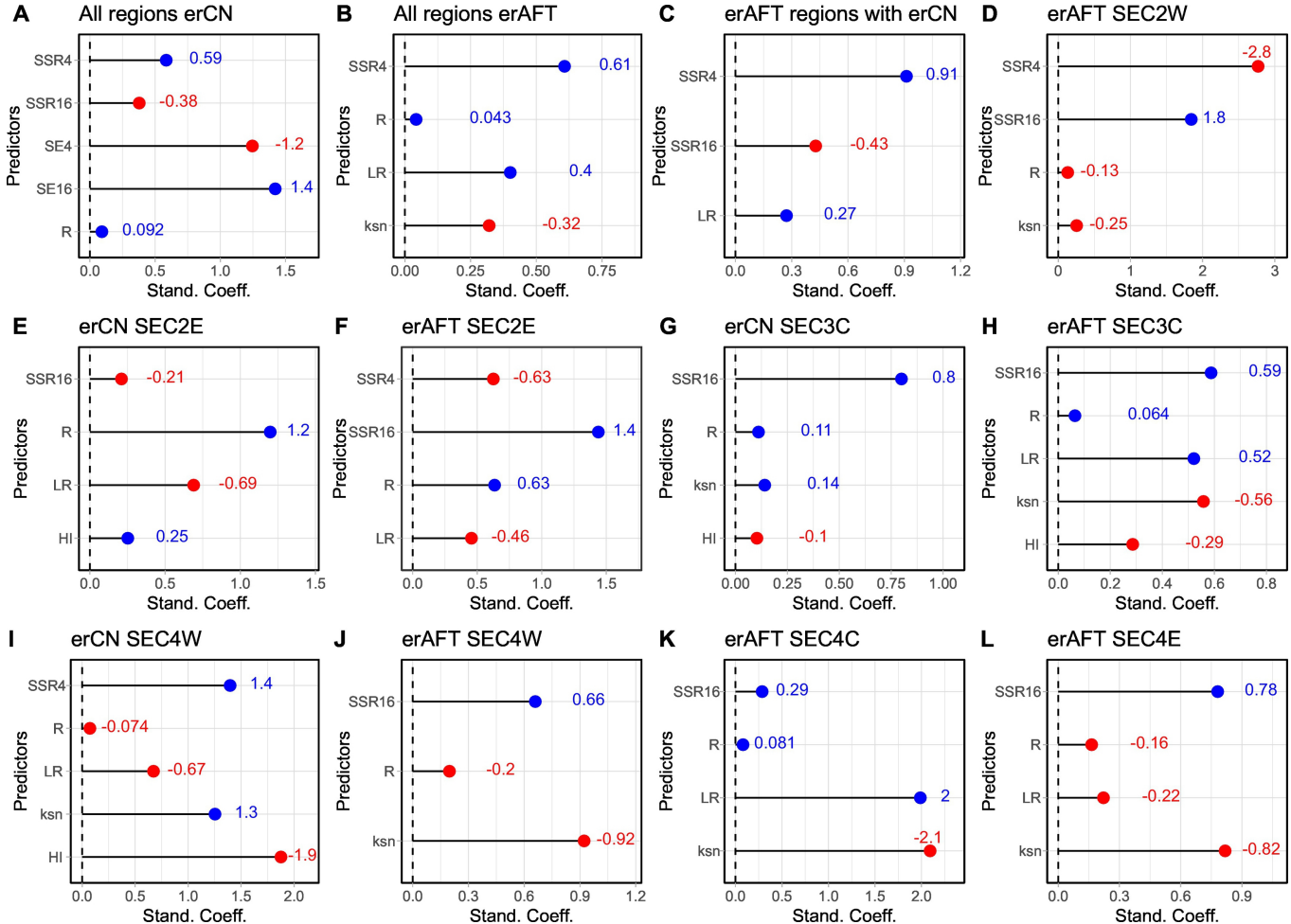
A
All regions erCN
SSR4
SSR16
SE4
SE16
R
0.59
-0.38
-1.2
1.4
0.092
Predictors
0.0 0.5 1.0 1.5
Stand. Coeff.
B
All regions erAFT
SSR4
R
LR
ksn
0.61
0.043
0.4
-0.32
Predictors
0.00 0.25 0.50 0.75
Stand. Coeff.
C
erAFT regions with erCN
SSR4
SSR16
LR
0.91
-0.43
0.27
Predictors
0.0 0.3 0.6 0.9 1.2
Stand. Coeff.
D
erAFT SEC2W
SSR4
SSR16
R
ksn
-2.8
1.8
-0.13
-0.25
Predictors
0 1 2 3
Stand. Coeff.
E
erCN SEC2E
SSR16
R
LR
HI
-0.21
1.2
-0.69
0.25
Predictors
0.0 0.5 1.0 1.5
Stand. Coeff.
F
erAFT SEC2E
SSR4
SSR16
R
LR
-0.63
1.4
0.63
-0.46
Predictors
0.0 0.5 1.0 1.5
Stand. Coeff.
G
erCN SEC3C
SSR16
R
ksn
HI
0.8
0.11
0.14
-0.1
Predictors
0.00 0.25 0.50 0.75 1.00
Stand. Coeff.
H
erAFT SEC3C
SSR16
R
LR
ksn
HI
0.59
0.064
0.52
-0.56
-0.29
Predictors
0.0 0.2 0.4 0.6 0.8
Stand. Coeff.
I
erCN SEC4W
SSR4
R
LR
ksn
HI
1.4
-0.074
-0.67
1.3
-1.9
Predictors
0.0 0.5 1.0 1.5 2.0
Stand. Coeff.
J
erAFT SEC4W
SSR16
R
ksn
0.66
-0.2
-0.92
Predictors
0.0 0.3 0.6 0.9 1.2
Stand. Coeff.
K
erAFT SEC4C
SSR16
R
LR
ksn
0.29
0.081
2
-2.1
Predictors
0.0 0.5 1.0 1.5 2.0
Stand. Coeff.
L
erAFT SEC4E
SSR16
R
LR
ksn
0.78
-0.16
-0.22
-0.82
Predictors
0.0 0.3 0.6 0.9
Stand. Coeff.

Figure 11

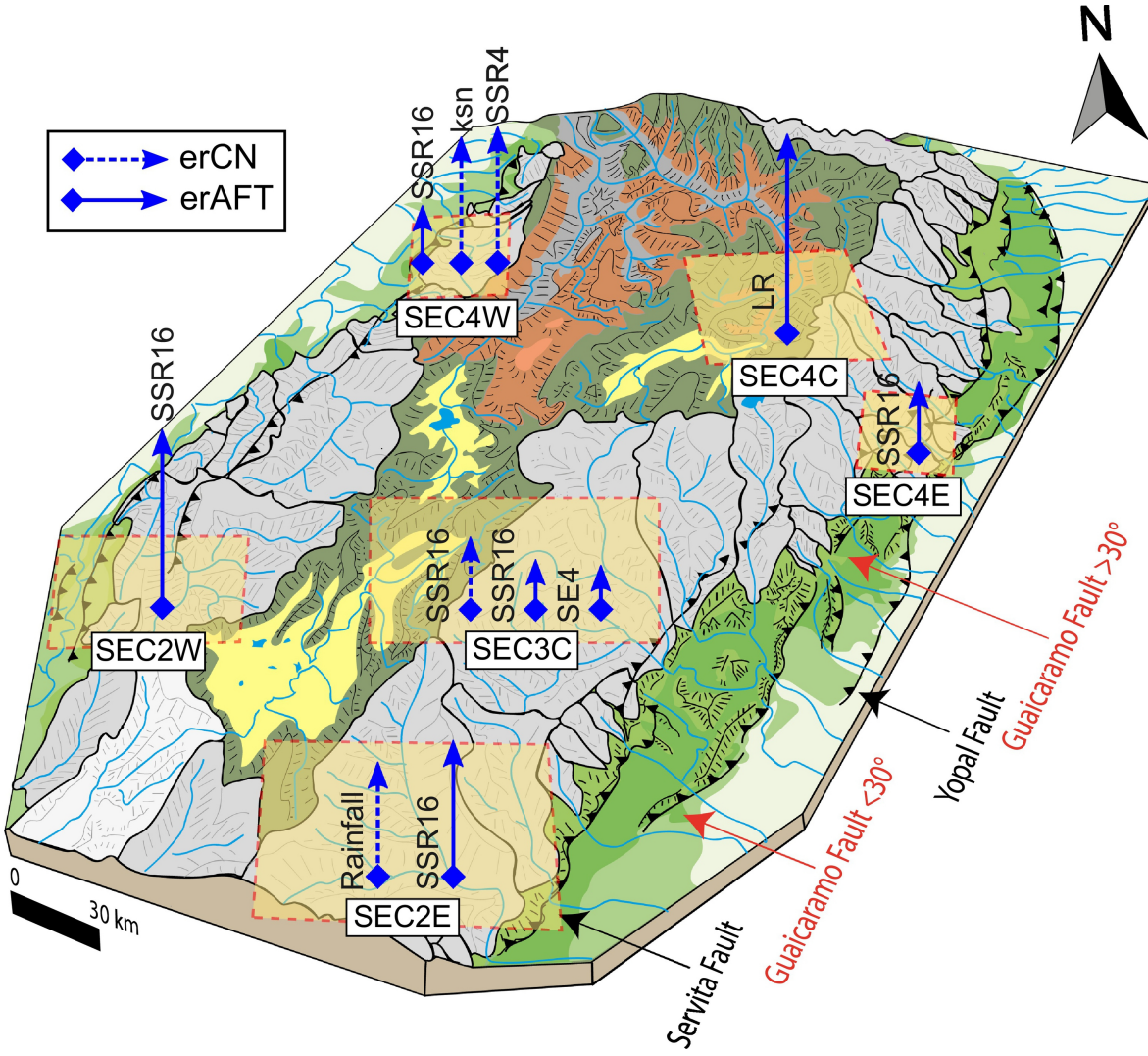
N
erCN
erAFT
SSR16
ksn
SSR4
SEC4W
LR
SEC4C
SSR16
SEC4E
SSR16
SEC2W
SSR16
SSR16
SE4
SEC3C
Rainfall
SSR16
SEC2E
0
30 km
Servita Fault
Guaicaramo Fault <30°
Yopal Fault
Guaicaramo Fault >30°

Figure 12

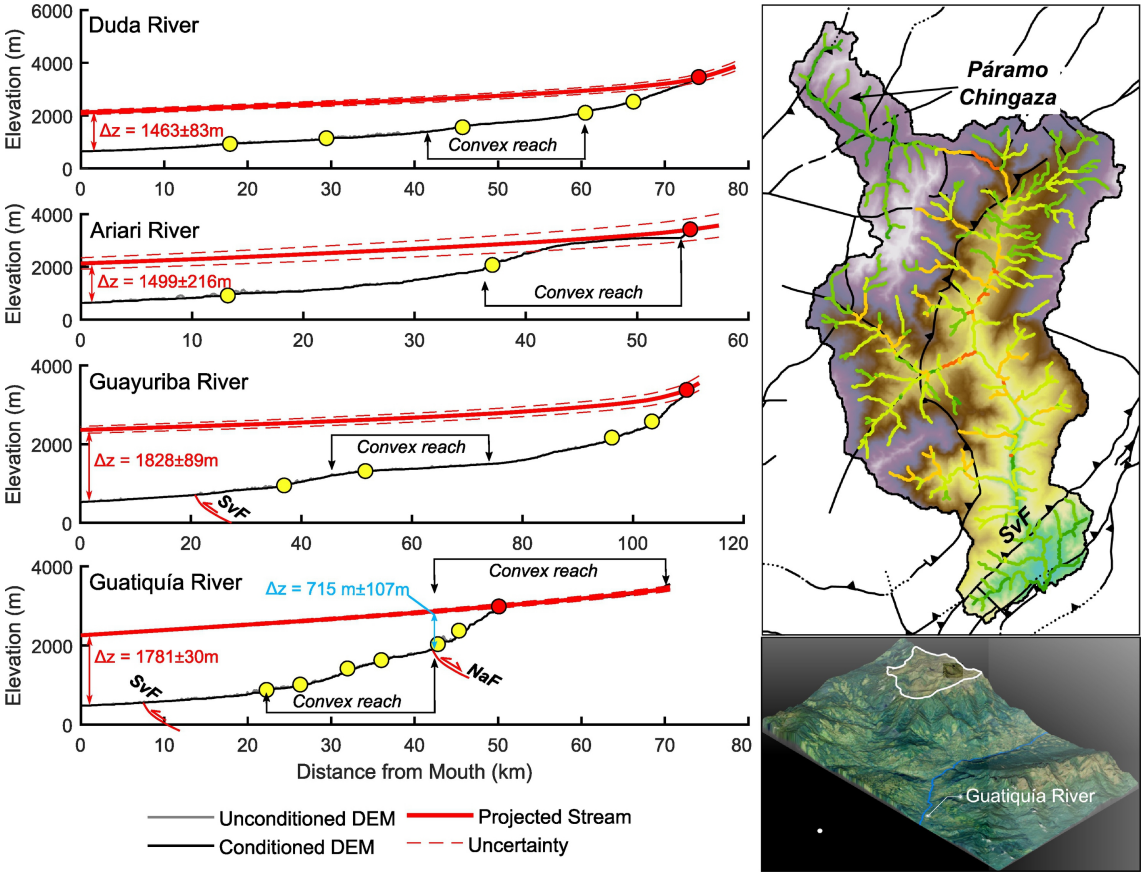
Duda River
Δz = 1463±83m
Convex reach
Ariari River
Δz = 1499±216m
Convex reach
Guayuriba River
Δz = 1828±89m
Convex reach
SvF
Guatiquía River
Δz = 715 m±107m
Convex reach
Δz = 1781±30m
SvF
NaF
Convex reach
Elevation (m)
Distance from Mouth (km)
Unconditioned DEM
Conditioned DEM
Projected Stream
Uncertainty
Páramo
Chingaza
SvF
Guatiquia River

Figure 13